ELSEVIER

Contents lists available at ScienceDirect

Geochimica et Cosmochimica Acta

journal homepage: www.elsevier.com/locate/gca





Trends in estuarine pyrite formation point to an alternative model for Paleozoic pyrite burial

Kalev Hantsoo^{a,*}, Maya Gomes^a, Dana Brenner^a, Jeffrey Cornwell^b, Cindy M. Palinkas^b, Sairah Malkin^b

- ^a Department of Earth and Planetary Sciences, Johns Hopkins University, 3400 N. Charles St., Baltimore, MD 21218, USA
- b Horn Point Laboratory, University of Maryland Center for Environmental Science, 2020 Horns Point Rd., Cambridge, MD 21613, USA

ARTICLE INFO

Associate editor: Elizabeth D. Swanner

Keywords: Pyrite Early Paleozoic Oxygen Bioturbation Chesapeake Bay

ABSTRACT

The early Paleozoic Era (~540-420 Ma) was an interval of profound biogeochemical changes including increasing oxygen (O2) and the onset of bioturbation (sediment mixing by animals). It is hypothesized that incipient bioturbation caused a monotonic decrease in sedimentary burial of pyrite (FeS2), which would have slowed atmospheric O2 accumulation. However, pyrite accumulation can exhibit complex responses to dynamic, low-O2 environmental conditions. To assess pyrite burial in a potential modern analogue to early Paleozoic environments, we collected sediment cores from the Chesapeake Bay, an estuary with multiple gradients in sulfate concentration, hypoxia intensity, organic carbon flux and lability, and bioturbation. Results indicate that pyrite accumulation is maximized not under strong sulfate depletion in highly reducing sediments, but rather in sediments that occupy the mid-range of sulfate-chloride ratios. This probably occurs through efficient replenishment of pore water sulfate and/or through the generation of sulfur redox intermediates, which promote pyrite formation via the polysulfide reaction pathway. In light of these results and in contrast to earlier models, we hypothesize that mild early Paleozoic bioturbation temporarily increased pyrite burial efficiency by stimulating higher sulfate reduction rates and increasing sedimentary sulfide retention. Compiled sulfur and carbon data from a geochemical database indicate that median sulfur-carbon ratios of fine-grained marine siliciclastic rocks increased from the Ediacaran through the Ordovician, then decreased and became much less variable from the Silurian onward. Thus, the Cambrian and Ordovician Periods may constitute a distinct interval of the Proterozoic-Phanerozoic transition in which bioturbation temporarily accelerated O2 buildup. This transition probably ended in the Silurian, when pO2 rose to sufficient levels to homogenize sedimentary carbon-sulfur cycling.

1. Introduction

The timing of Earth system oxygenation and its links to biological evolution are central questions in geobiology (Cole et al., 2020; Sperling et al., 2022). Oxygen (O₂) accumulation at Earth's surface has primarily resulted from the reduction of carbon dioxide (CO₂) via oxygenic photosynthesis and the reduction of sulfate (SO_4^2) via microbial sulfate reduction, followed by reduced carbon and sulfur burial (Holland, 1962; Holland, 1973). Net oxidation of the ocean—atmosphere system occurs if the reduced products of these reactions—organic carbon and sulfide, respectively—are separated from the oxidized products by burial in sediment; otherwise, the reverse reactions will consume the oxidized species (Garrels and Perry, 1974). Sedimentary pyrite (FeS₂) is the largest stable

reservoir of sulfide in crustal sediments (Rickard and Luther, 2007), although organosulfur compounds can also become a significant component of reduced sulfur in association with sulfur redox intermediates (Riedinger et al., 2017), or in localities with very high organic carbon content (Zaback et al., 1993). Given that the reduction of sulfate followed by sedimentary pyrite burial has been one of the two major sources of ocean–atmosphere oxygenation over Earth's history (Berner, 1982), increases in the global rate of pyrite precipitation and burial in Earth's past would have quickened the pace of $\rm O_2$ buildup.

The availability of organic carbon, sulfate, and reactive iron have commonly been cited as the primary controls on the rate of sedimentary pyrite accumulation (Berner, 1984). Pyrite burial in many modern localities is roughly proportional to burial fluxes of total organic carbon (TOC),

E-mail address: khantso1@jhu.edu (K. Hantsoo).

^{*} Corresponding author.

with a TOC/pyrite-S ratio of 2.8 \pm 0.8 attributed to 'normal marine' sediments, i.e. sediments that are deposited under oxygenated marine waters with normal ocean salinity of ~35 (Berner, 1982; Berner and Raiswell, 1983). This relationship exists primarily because organic carbon deposition rates broadly fuel and quantitatively scale with sediment microbial sulfate reduction rates, although it is not only the amount of TOC but also TOC reactivity that plays a role in determining sulfate reduction rates (Meister et al., 2013). Up to 90 % of the sulfide produced by microbial sulfate reduction is reoxidized (Jørgensen, 1982), and the amount of sulfide buried as pyrite is influenced by the favorability of three pyrite-forming reactions. Pyrite typically forms by the reaction of iron monosulfide (FeS) with either hydrogen sulfide (H₂S) or polysulfide (S_n²⁻, where $2 \le n \le 8$) (Luther, 1991; Rickard and Luther, 1997; Butler et al., 2004); alternatively, pyrite can form via the reaction of ferric hydroxide surface species with dissolved sulfide to yield Fe(II)OH₂⁺, which then reacts with sulfide or polysulfide radicals to form pyrite (Wan et al., 2017). This latter reaction is called the ferric hydroxide surface (FHS) pathway and is most favorable under high ratios of Fe(III)-oxide minerals to dissolved sulfide (Wan et al., 2017).

Polysulfides are a pool of reduced sulfur that forms through the reaction of dissolved bisulfide (HS $^-$) with elemental sulfur (S₈) and exists in equilibrium with these species (Teder, 1971; Steudel, 2003). Higher pH in anoxic pore water will favor the generation of HS $^-$ and polysulfides, while lower pH will favor the generation of H₂S and S₈ (Kamyshny et al., 2003, 2004). The two FeS-derived pyrite formation pathways follow the form.

$$S_n^{2-} + FeS \rightarrow S_{n-1}^{2-} + FeS_2$$
 (1)

$$H_2S + FeS \rightarrow H_2 + FeS_2$$
 (2)

with Eq. (1) referred to as the polysulfide pathway (where n commonly ranges from 4 to 6 under relevant environmental conditions; Kamyshny et al., 2004) and Eq. (2) referred to as the H₂S pathway. In Eq. (1), n refers to the number of sulfur atoms in a polysulfide molecule.

Although pyrite formation is associated with reducing environments, Eqs. (1) and (2) demonstrate that pyrite sulfur (with an oxidation state of -1) is more oxidized than FeS sulfur (with an oxidation state of -2). The oxidative power in Eq. (1) derives from the internal sulfur atoms in polysulfide, which have formal oxidation states of 0. Meanwhile, in Eq. (2), H_2S completes FeS-pyrite oxidation by reducing its hydrogen to molecular hydrogen (H_2) (Rickard, 2012). The FHS pathway involves net oxidation of sulfide via the surfaces of ferric hydroxide minerals, generating sulfide or polysulfide radicals with a -1 oxidation state which can then participate in pyrite nucleation (Wan et al., 2017).

It was previously thought that partially oxidized sulfur compounds might be a necessary component of pyrite precipitation (Berner, 1970; Berner, 1974), but the demonstration of the H₂S pathway at ambient temperatures (Drobner et al., 1990; Rickard, 1997; Schoonen, 2004) indicated that pyrite precipitation can occur via a simpler set of reactions, since the presence of H₂S requires only sulfate reduction rather than an oxidative sulfur cycle. Because polysulfide is a mixed-valence sulfur species that requires relatively alkaline conditions and H₂S is a reduced species that exists under relatively acidic conditions, it is generally assumed that the H₂S pathway predominates in strongly reducing and acidic environments while the polysulfide pathway predominates under slightly more oxidized and alkaline conditions (Rickard and Luther, 2007). The FHS pathway has been proposed as a significant reaction in sediments with high fractions of reactive iron and low amounts of sulfide, e.g., in low-salinity systems with high terrigenous sediment loads (Wan et al., 2017).

The relative rates of the $\rm H_2S$ and polysulfide reaction pathways are difficult to constrain, but sulfur cycling microorganisms—including sulfate reducing, sulfide oxidizing, and sulfur disproportionating microbes—are critical to both reactions. Although abiotic laboratory experiments have generated reaction rate constants that indicate that the $\rm H_2S$ pathway is substantially faster than the polysulfide pathway (Butler et al., 2004), experiments that include microbial activity suggest roughly equal fluxes of pyrite formation via these two pathways in natural settings (Canfield et al., 1998). The rate limiting step of Eqs. (1) and (2) is pyrite nucleation, which requires supersaturated conditions and can be strongly influenced by

microbial activity (Schoonen and Barnes, 1991; Canfield et al., 1998; Rickard and Luther, 2007; Rickard, 2012). The most obvious influence of microbial sulfur metabolisms on pyrite formation is their generation of H_2S and sulfur redox intermediates; however, microbial biomass itself can also aid in the precipitation of pyrite and FeS (Donald and Southam, 1999; Wacey et al., 2015; Picard et al., 2018; Duverger et al., 2020), and microbial interactions can promote pyrite formation (Thiel et al., 2019).

A further complication in deciphering the rate of Eq. (1) is that polysulfide is a highly reactive compound that is sensitive to electron activity (Eh) and proton activity (pH) (Kleinjan et al., 2005a). Furthermore, the generation of polysulfide to fuel Eq. (1) likely depends on the surface areas of S₈ and FeS, which are also difficult to measure (Rickard, 1975). The solubility of S₈ also influences pore water polysulfide concentration, but the rate of reaction of S₈ with the dissolved sulfide-polysulfide pool can vary by ~6 orders of magnitude depending on whether S₈ is in dissolved, colloidal, or crystalline form (Fossing and Jørgensen, 1990; Kamyshny and Ferdelman, 2010; Avetisyan et al., 2019). Sulfur-cycling metabolisms can influence this aspect of pyrite precipitation because sulfide oxidizing microbes such as Beggiatoa can generate large amounts of colloidal, watersoluble S₈ globules by encasing them in hydrophilic proteins (Kleinjan et al., 2005b; Maki, 2013). This hydrophilicity can increase the rate of the reaction of S₈ with HS⁻ to form polysulfide. Thus, although the rates of Eqs. (1) and (2) are difficult to constrain in natural environments, it is apparent that microbial oxidative sulfur cycling plays an important role in determining rates of pyrite formation because of its strong influence on the concentrations of H_2S , S_8 , and S_n^{2-} in sediments.

The response of pyrite precipitation rates to changing sediment and water column conditions is important to our understanding of the early Paleozoic Era, which spans the beginning of the Cambrian Period through the end of the Silurian Period (~540–420 Ma; Tarhan et al., 2021). The redox proxy record of this interval of Earth history is somewhat ambiguous but generally points to lower atmospheric oxygen concentrations than those of the modern Earth system (Tostevin and Mills, 2020; Wei et al., 2021), a conclusion that is supported by recent generations of Earth system box models (Krause et al., 2018; Lenton et al., 2018). The pace of oxygenation in the early Paleozoic is important for contextualizing the remarkable evolutionary changes that occurred in this interval, including the spread of biomineralization (Wood and Zhuravlev, 2012), the restructuring of trophic networks (Dunne et al., 2008), the diversification of animal body plans (Knoll and Carroll, 1999), and the onset of penetrative bioturbation (Bottjer et al., 2000; Carbone and Narbonne, 2014).

Bioturbation, the physical mixing and fluid exchange of shallow sediments caused by animals (Kristensen et al., 2012), has increasingly influenced biogeochemical cycling across the Phanerozoic Eon. In the modern Earth system, bioturbation has a pronounced effect on sedimentary biogeochemistry (Meysman et al., 2006; Deng et al., 2020; van de Velde et al., 2020). Its advent in the Paleozoic Era has been implicated in changes to the cycling of phosphorus (Boyle et al., 2014; Tarhan et al., 2021), iron (van de Velde et al., 2023), and sulfur (Canfield and Farquhar, 2009). The rate at which early bioturbation intensified is a critical factor in understanding its effect on the biogeochemical evolution of Paleozoic Earth. Sediment fabric analysis indicates that the sedimentary mixed layer deepened only gradually from the Cambrian onward, reaching ~1.5 cm by the Silurian and ~3 cm by the Devonian—well short of the modern global mixed layer depth of ~10 cm (Tarhan et al., 2015; Boudreau, 1998). It is possible that the initial deepening of the sedimentary mixed layer could have had a disproportionately large effect on sediment biogeochemistry, but the likelihood of a nonlinear response to early penetrative bioturbation has been questioned (Cribb et al., 2023). On the other hand, sedimentary oxidative sulfur cycling can undergo complex responses to bioturbation, such as ecological turnover between sulfide oxidizing communities of Beggiatoa and cable bacteria (Malkin et al., 2022).

Bioturbation has been shown to stimulate sulfate reduction. High sulfate reduction rates are frequently observed in sediments with moderate to strong bioturbation (Goldhaber et al., 1977; Aller and Yingst, 1978; Jørgensen and Parkes, 2010; Quintana et al., 2013; Jørgensen, 2021). Sulfate reduction rates have also been shown to be substantially higher in

bioturbated sediments than in nearby or otherwise similar non-bioturbated sediments (Hines and Jones, 1985; Bertics et al., 2010; Bertics and Ziebis, 2010; cf. Kristensen and Blackburn, 1987; Nielsen et al., 2003), including in the Chesapeake Bay (Roden and Tuttle, 1993). This probably occurs because bioirrigation (i.e., fluid advection) introduces fresh sulfate to the substrate, while biodiffusion (i.e., solid particle diffusion) simultaneously mixes labile organic matter downward as a reductant to fuel further sulfate reduction (van de Velde and Meysman, 2016). In other words, bioturbation can increase the supply of sulfate to sediments while also increasing microbial sulfate demand.

The effect of bioturbation on sedimentary sulfide retention, i.e. 'net' sulfate reduction (Moeslund et al., 1994), is more ambiguous because bioturbation introduces dissolved oxygen and solid oxide compounds to the substrate (Thamdrup et al., 1994). Dissolved oxygen can quickly oxidize H₂S, pyrite, and FeS (Lowson, 1982; Zhang and Millero, 1993; Jeong et al., 2010); Fe-oxides oxidize H₂S to ZVS (Poulton et al., 2004); and MnO₂ oxidizes pyrite to sulfate, FeS to ZVS, and H2S to polysulfide (Schippers and Jørgensen, 2001; Avetisyan et al., 2021). Moderate bioturbation has minimal effects on the oxygen penetration depth of sediments, but it can increase the thickness of the suboxic layer, typically defined as the zone in which neither O₂ nor dissolved sulfide are present (Bonaglia et al., 2019; Cribb et al., 2023). Thus, the net effect of oxidant mixing on pyrite formation and retention depends on the mode and intensity of bioturbation. If bioturbation and net mixed layer oxidation are mild, then the addition of Fe- and Mn-oxides may promote pyrite precipitation by partially oxidizing sulfides to sulfur redox intermediates, including polysulfides. Under more strongly oxidizing conditions, sulfide compounds (both solid and dissolved) are more likely to be fully reoxidized to sulfate.

Pioneering studies of sedimentary pyrite formation in the modern environment generally focused on 'end-member' settings, i.e., sediments with well-developed mixed layers under generally oxic water (Goldhaber et al., 1977; Jørgensen, 1977) or non-burrowed sediments underlying permanently sulfidic water (Lyons, 1997). However, settings with low rates of bioturbation and fluctuating oxygen concentration may more closely reflect the conditions that prevailed along continental shelves and slopes in the early Paleozoic (Tarhan et al., 2015; Pruss and Gill, 2024). Emerging models of early Paleozoic ocean redox evolution point to the establishment of wedge-shaped, fluctuating oxygen minimum zones over mid-shelf sediments, with inner and outer shelf sediments less prone to anoxia (Guilbaud et al., 2018). Trace fossil distributions from inner to outer shelf facies corroborate this model (Buatois et al., 2020). Combined fossil and geochemical data suggest that oxic-euxinic oscillations occurred on submillennial timescales in a Cambrian epicontinental sea (Dahl et al., 2019), and distinct sediment cores from the same basin (separated by ~150 km) may reflect different contemporaneous concentrations of water column H2S between sites (Zhao et al., 2023). Localized variability in continental shelf oxygenation is also documented into the Ordovician and Silurian (Edwards et al., 2018; Jin et al., 2021).

Given the emerging picture of Paleozoic shallow marine redox structures, studies of present-day pyrite formation in more heterogeneous redox regimes—particularly upwelling zones (Böning et al., 2004) and semi-restricted hypoxic basins (Figueroa et al., 2023; Liu et al., 2021)—may provide a better analog for geochemical conditions that prevailed in the early Paleozoic. In this intermediate redox category, the Chesapeake Bay presents a distinctive case of rapid redox fluctuation. Even the most oxygen-stressed areas of the Chesapeake Bay, which feature no bioturbation and undergo months of anoxia/euxinia each year, are still exposed to oxic bottom waters a majority of the time and retain median annual benthic oxygen concentrations of at least 4 mg/L (Table 1). Although these fluctuations are unusual for a modern shallow marine basin, they may have been more common in the early Paleozoic, when lower atmospheric pO₂ made shallow marine water columns more susceptible to spatiotemporal redox variability (Pruss and Gill, 2024).

For the purposes of understanding the pace of Paleozoic oxygenation, controls on shallow marine pyrite burial play a larger role in determining global pyrite burial fluxes than controls on deep marine pyrite burial. This is because pyrite burial broadly scales with organic carbon burial, and

about 85 % of modern marine organic carbon burial occurs in shelf and deltaic sediments (Hedges and Keil, 1995); in the Paleozoic world, when pelagic primary productivity was lower than today (Ridgwell and Zeebe, 2005), this fraction may have been higher. Furthermore, the majority (76 %) of global sulfate reduction occurs in shallow (<200 m) marine environments (Canfield et al., 2005). If lower slope environments (200–1000 m) are also included, sulfate reduction in shallow settings constitutes 94 % of global sulfate reduction (Canfield et al., 2005). In light of the complex relationships between bioturbation, microbial oxidative sulfur cycling, and pyrite precipitation rates, it is important to investigate trends in shallow marine pyrite burial under dynamic, low-oxygen conditions similar to the early Paleozoic.

2. Methods

2.1. Study site characterization

Early Paleozoic oxygen concentrations were likely 30-40 % of present atmospheric level (PAL) until the middle to late Silurian, with thick oxygen minimum zones predominating in marine shelf/slope environments (Tostevin and Mills, 2020). Therefore, it is useful to analyze biogeochemical cycling in modern basins that provide low-oxygen—but not fully anoxic—analogs to early Paleozoic environments. In particular, the sensitivity of pyrite and its precursor compounds to spatiotemporal fluctuations in redox conditions merits further investigation. The Chesapeake Bay, a large estuary formed by the inundation of the lower Susquehanna River basin after the Last Glacial Maximum (Colman et al., 1990), provides an excellent study site for comparison to early Paleozoic biogeochemistry. Seasonal oxygen depletion has affected the Chesapeake Bay for decades, particularly in the relict Susquehanna River channel that runs north-south through the center of the Bay (Newcombe and Horne, 1938; Cooper and Brush, 1991; Kemp et al., 2005). Oxygen depletion affects the infaunal activity of bioturbating organisms, leading to year-round inhibition or elimination of bioturbation in parts of the Bay, especially in and near the central channel; other parts of the Bay are lightly burrowed for only part of the year (Schaffner et al., 1992; Marvin-DiPasquale and Capone, 1998). The deeper reaches of the water column in the central channel regularly become euxinic (i.e., anoxic and bearing dissolved sulfide) during the peak of summer hypoxia (i.e., dissolved oxygen concentrations <63 µM; Roden and Tuttle, 1992; Findlay et al., 2015).

The extreme oxygen depletion in certain parts of the Chesapeake Bay results from a confluence of several factors. First, the bathymetry of the Bay inhibits vertical mixing in the central channel (Wang et al., 2016); second, a two-layer estuarine circulation regime results in stratification of dense, tidally pumped seawater flowing northward from the Bay's mouth underneath freshwater flowing south from the Susquehanna River (Pritchard, 1952); third, anthropogenic nutrient input promotes eutrophication (Hagy et al., 2004). These factors combine to create overlapping spatiotemporal gradients in salinity, sedimentation rate, intensity and duration of hypoxic episodes, bioturbation, and the amount and reactivity of organic carbon reaching the sediments. The Chesapeake Bay thus presents a natural laboratory in which to study pyrite accumulation under fluctuating redox conditions, which may have typified shallow marine sediments in the early Paleozoic (Tostevin and Mills, 2020).

To investigate the impact of low and variable benthic oxygen conditions on pyrite burial, we selected nine sites (Fig. 1) that have been regularly monitored for water column chemistry since 1984. The compiled monitoring data are available from the Chesapeake Bay Program Water Quality Database (https://www.chesapeakebay.net/what/downloads/cbp-water-quality-database-1984-present). Selected site characteristics are presented in Table 1. We note that Chesapeake Bay Program monitoring sites in the mainstem of the Chesapeake Bay are given the prefix "CB," but because all of the sites in this study are in the mainstem, we have omitted this prefix from site names. The sites were chosen to reflect a wide range in the parameters that can affect sedimentary sulfur cycling, including sulfate concentration (as determined by salinity), hypoxia intensity, organic carbon flux and lability, sedimentation rate, and bioturbation rates. Generally,

Table 1Site characteristics.

Station ID	Water depth (m) ⁽¹⁾	Coordinates ⁽¹⁾	Mean annual surface salinity ⁽²⁾	Mean annual bottom water salinity ⁽²⁾	Days yr^{-1} below 0.3 mg O_2 L^{-1} (2)	Mean annual benthic [O ₂] (mg/ L) ⁽²⁾	Sediment Mixed Layer Depth (cm) ⁽³⁾	Surficial Sediment Grain Size ^(4,5)
3.1	8	39 14.97N, 76 14.42W	4.2	11.1	5	6.0	2 (1–3)	Clayey silt
3.2	10	39 09.779N, 76 18.386W	6.5	13.0	17	5.3	6 (5–8)	Silty clay to clayey silt
3.3C	24	38 59.757N, 76 21.573W	9.2	17.2	72	4.2	0	Silty clay
3.3W	8.4	39 00.281N, 76 23.380W	9.3	13.4	6	6.4	2.25 (1.5–3)	Silty clay
4.3C	22	38 33.284N, 76 25.774W	12.2	19.2	59	4.7	0	Silty clay
4.3W	8.7	38 33.437N, 76 29.641W	12.4	13.4	12	7.7	4 (3.75–4.25)	Clay to silty clay
5.1C	35	38 19.122N, 76 17.522W	13.6	20.0	44	5.1	1 (0–2)	Silty clay
5.1W	15	38 21.050N, 76 20.519W	13.2	14.3	3	8.1	7 (7–10)	Fine sand to silty clay
5.5	17	37 41.497N, 76 11.382W	16.0	20.8	5	6.9	0.75 (0-1)	Clayey silt

¹ Measured during core collection.

northern sites have lower water column sulfate concentration and a higher flux of terrigenous organic carbon than southern sites (Zimmerman and Canuel, 2001). Compared to the northern and southern Bay, the mid-Bay region features a minimum in clastic sediment deposition and a maximum in productivity that contributes to lower benthic oxygen concentrations (Officer et al., 1984; Harding et al., 1986). The central channel sites (denoted with the suffix "C") are much more susceptible to prolonged O_2 depletion than the western shoal sites (denoted with the suffix "W"). In this study, we measured the concentration and isotopic composition of pyrite, pyrite-forming sulfur compounds, and organic carbon in sediment cores from the nine sites. Our goals were to understand the processes that influence pyrite burial under low and variable benthic oxygen concentrations and to inform models of early Paleozoic oxygenation.

2.2. Core collection and initial processing

Eight of the nine analyzed cores were collected from July 22–24, 2019 on the R/V Rachel Carson; the ninth core was collected from site 4.3W on August 11, 2021 on the same vessel. Cores were collected in 6.8 cm diameter tubes with a gravity corer, sealed aboard ship, and sectioned under N_2 at the University of Maryland Center for Environmental Science, Horn Point Laboratory (UMCES-HPL; Cambridge, MD) for the cores collected July 22–24, 2019 and at Johns Hopkins University (JHU; Baltimore, MD) for the core collected on August 11, 2021. Cores were sectioned in an N_2 -purged glovebag at a resolution of 1 cm in the top 10 cm, 2 cm from 10–20 cm depth, and 5 cm at depths below 20 cm, except for the top 5 cm of 4.3W, which was sectioned at 0.5 cm resolution. Extruded samples were placed in centrifuge tubes, sealed with Parafilm, and centrifuged for 25 min at 4200 RPM to remove pore water. Samples were then returned to an N_2 -purged glovebag where pore waters were removed and sediment samples were sealed in foil barrier bags and stored at $-20\,^{\circ}$ C.

2.3. Sulfur species concentrations

Sequential extractions of solvent-extractable sulfur (SES, which primarily consists of elemental sulfur and other zero-valent sulfur species), acid-volatile sulfur (AVS, which primarily consists of iron monosulfides) and chromium-reducible sulfur (CRS, which primarily consists of pyrite) were conducted after the methods of Liu et al. (2020). Elsewhere in this

paper, 'pyrite' refers to the CRS fraction extracted after ZVS and AVS extractions, 'FeS' refers to the AVS fraction, and 'ZVS' (zero-valent sulfur) refers to the SES pool. Two aliquots of equal volume (0.2–0.4 mL wet volume) were extracted from each sample tube under N_2 , with the first aliquot placed in a 70 °C oven for 24 h and then weighed. The second aliquot was placed in a centrifuge tube with 1.0 mL of a N_2 -purged 3 % Zn acetate / 0.1 M acetic acid solution and 5.0 mL of N_2 -purged 3:1 methanol: toluene. These tubes were wrapped in Parafilm, sealed inside foil barrier bags, and reacted on a shaker table for 18 h at 150 RPM to allow zero-valent sulfur to dissolve into the organic solvent. After shaking, the tubes were centrifuged at 4200 RPM for 25 min; then, under N_2 , the supernatant solvent and the sediment were removed from each tube into separate round-bottom flasks.

The sediment fraction of each sample was then subjected to sequential AVS-CRS extractions. To extract AVS, the sediment in each round bottom flask was reacted with 40 mL of $N_2\text{-purged}$ 6N HCl for 2 h at 70 $^{\circ}\text{C}$ under N_2 carrier gas. Produced H₂S gas was bubbled through a solution of 3 % Zn acetate/0.1 M acetic acid and trapped as zinc sulfide. Once the AVS extraction was complete, 40 mL of 1 M CrCl₂/0.5 M HCl was added to the same flask to react with the CRS fraction at 70 °C for 2 h, with product H₂S trapped again as zinc sulfide. The produced zinc sulfides were then converted to silver sulfide (Ag₂S) with excess silver nitrate. The supernatant solvent containing dissolved SES was subjected to a separate CRS extraction with 20 mL of N_2 -purged 6N HCl and 30 mL of 1 M CrCl₂ / 0.5 M HCl. These solutions were injected into the flask simultaneously and then reacted with the solvent for 2 h at 70 °C. All produced Ag₂S samples were rinsed with 1 M NH₄OH (Firsching, 1961), triple-rinsed with deionized water, dried at 70 °C, and weighed on a microbalance to determine sulfur species concentrations.

Based on sets of duplicate extractions, the standard error $(\sigma/\sqrt{2})$ for concentration of SES, AVS, and CRS was 0.01 %, 0.03 %, and 0.03 % respectively (absolute difference), or 17 %, 11 %, and 5 % (relative difference). Absolute differences in measured abundance between SES replicates were fairly consistent (typically 0.01–0.02 %) regardless of sample yield, meaning that relative precision increased at higher SES abundances.

After the initial centrifuging of samples during core extrusion, pore water samples for determination of $\rm H_2S$, sulfate, and chloride concentration were pipetted in aliquots of 1.40 mL into two microcentrifuge tubes containing 0.10 mL of 3 % zinc acetate to form zinc sulfide and inhibit microbial activity. These samples were stored in their tubes at 4 $^{\circ}C$ until

² Data collected from Chesapeake Bay Program Water Quality Database and averaged after spline interpolation.

³ Estimated from observations of collected sediment cores and/or from previous publications; details for each core are presented in the Supplementary Information. Potential ranges are expressed in parentheses.

⁴ Kerhin et al. (1988).

⁵ Byrne et al. (1982).

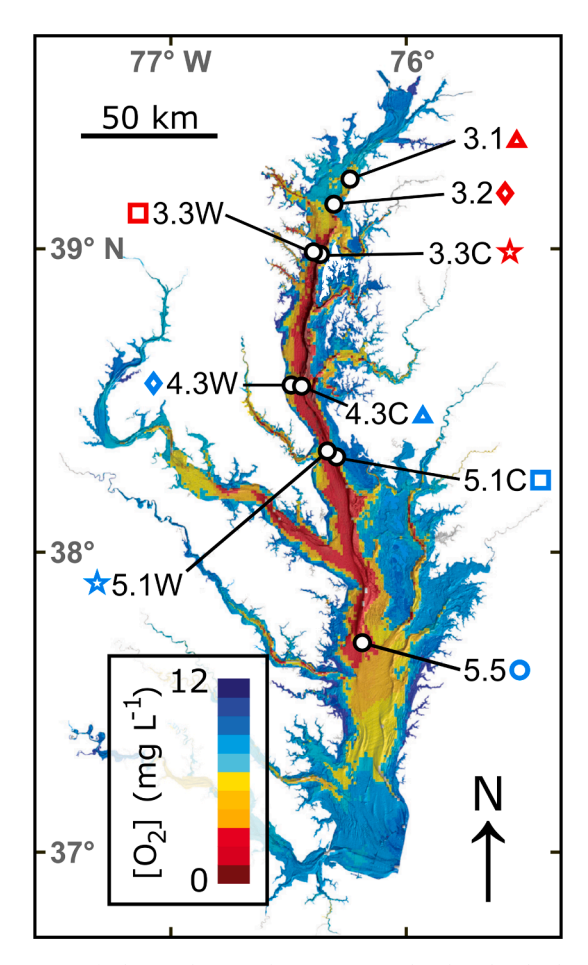


Fig. 1. Map of Chesapeake Bay depicting mean benthic dissolved oxygen concentrations from summer 2005 (Wicks et al., 2007). Locations of core sites are denoted with white markers. Colored symbols next to site names are used in subsequent figures to denote each site.

further analysis. One set of samples was subjected to AVS extractions as described above under 40 mL of 6N HCl at 70 $^{\circ}\text{C}$ for 2 h. The resulting silver sulfides were weighed on a microbalance to determine pore water H_2S concentrations.

Pore water sulfate and chloride concentrations for core 4.3W were measured at JHU, and those of the remaining eight cores were measured at UMCES-HPL. At JHU, pore water sulfate and chloride concentrations were measured by ion chromatography on a Dionex ICS-2100 Ion Chromatograph system using a Dionex AS18 column and KOH eluent. At UMCES-HPL, concentrations were measured on a Dionex ICS-2000 Ion Chromatograph system using a Dionex AS11-HC column and KOH eluent. Based on four duplicate extractions, the standard error for pore water anion concentrations was 1.2 % for sulfate and 1.6 % for chloride (relative difference).

2.4. Sulfur isotope analyses

Silver sulfide samples were weighed into tin capsules in aliquots of 200–400 μg along with 2.0–4.0 mg of vanadium pentoxide to ensure full combustion. These capsules were combusted at 1020 °C in a Thermo Scientific EA Isolink elemental analyzer, from which produced SO_2 was analyzed for sulfur isotope composition on a Thermo Scientific Delta V Plus Isotope Ratio Mass Spectrometer (IRMS) via a Conflo IV in continuous flow mode. Sulfur isotope ratios of samples were calibrated to the international standards IAEA-S1, IAEA-S2, and IAEA-S3, as well as an in-house Ag_2S standard. All sulfur isotope ratios are reported on the Vienna Canyon Diablo Troilite (VCDT) scale in delta notation $(\delta^{34}S) = [(^{34}S)^{32}S)_{sample}/(^{34}S)^{32}S)_{VCDT} - 1] * 81000)$. The standard error of measurements of

duplicate Ag₂S samples (i.e., the IRMS analytical error) was 0.24 ‰; the standard error of δ^{34} S analyses of duplicated extractions (which includes the IRMS analytical error) was 0.42 ‰, 0.38 ‰, and 2.2 ‰ for AVS, CRS, and SES respectively.

2.5. TOC analysis and $\delta^{13}C$ analyses

Sequential extraction residuals were triple-rinsed, dried, homogenized, and analyzed for $\delta^{13} C$ composition and TOC concentrations on a Thermo Scientific Delta V Plus IRMS via Conflo IV in continuous flow mode coupled to a Thermo Scientific EA Isolink elemental analyzer. The extraction process does not affect $\delta^{13} C$ values of organic carbon (Muller et al., 2017). All $\delta^{13} C$ values of TOC are reported relative to the Vienna Pee Dee Belemnite (VPDB) isotopic standard. Weight percent TOC measurements had a standard error of 0.58 % (absolute difference). Measurements of $\delta^{13} C$ based on replicated AVS-CRS extractions had a standard error of 0.80 ‰, which included the IRMS standard error of 0.12 ‰.

2.6. Radiotracer analyses

Sedimentation rates were calculated from ²¹⁰Pb (half-life 22.3 years) and ¹³⁷Cs (half-life 30.7 years). Both radioisotopes have been used in many estuarine systems, including the Chesapeake Bay, to calculate decadal-scale sedimentation rates (e.g., Colman et al., 2002; Rabalais et al., 2007; Russ and Palinkas, 2020). ²¹⁰Pb is a naturally occurring radioisotope produced by the decay of ²³⁸U and supplied to the water column by runoff, precipitation, and decay of its effective parent ²²⁶Ra. For ²¹⁰Pb and ¹³⁷Cs analysis, sediment aliquots were dried in an oven at 70 °C for 48 h and homogenized in an agate mortar. ²¹⁰Pb activities were determined at UMCES-HPL via gamma spectroscopy of the 46.5 keV photopeak, using calibrated germanium detectors, following Palinkas and Koch (2012). Total activities were calculated after applying a self-absorption correction (Cutshall et al., 1983) and decay-corrected to the time of core collection. Background activities from the decay of $^{226}\mathrm{Ra}$ were calculated from a weighted average of the ²¹⁴Pb (295.3 and 351.9 keV) and ²¹⁴Bi (609.4 keV) photopeaks. Excess ²¹⁰Pb activities were then calculated by subtracting the background activity from the total activity. Sediment accumulation rates were calculated with the constant flux/constant sedimentation (CFCS) model, which assumes steady-state sedimentation (Appleby and Oldfield, 1978). ¹³⁷Cs is a bomb-produced radionuclide and is present in sediments deposited since the onset of atmospheric nuclear weapon testing in 1954, with peak activities occurring in 1963 during maximum fallout. ¹³⁷Cs activities were calculated from the 661.6 keV photopeak of the gamma spectrum and decay-corrected to the time of core collection.

3. Results

3.1. Sulfur species concentrations

Pyrite sulfur concentrations ranged from 0.08 % to 2.21 % across all samples (all solid phase concentrations are reported as dry weight percent). Three sites (3.3W, 5.1C, and 5.1W) had pyrite concentrations that stayed nearly constant with depth, three other sites (4.3C, 4.3W, and 5.5) showed either stepwise or gradual increases in pyrite concentration with depth, and three northern sites (3.1, 3.2, and 3.3C) showed clear peaks in pyrite concentration between 10 and 20 cm depth (Fig. 2). Pyrite concentrations in all cores generally exceeded FeS and ZVS concentrations.

FeS concentrations ranged from <0.01 % to 0.87 % across all samples. FeS concentration was higher and more variable with depth at the four northern sites than at the five southern sites (Fig. 2). At the five southern sites, FeS concentrations were highest near the sediment–water interface and declined in the top 5–10 cm; the only exception was site 5.1C, at which FeS concentrations were low (<0.10 %) but did not decline with depth. FeS concentrations and FeS/pyrite-S ratios were highest at the four northernmost sites, which were substantially more sulfate-depleted than the other sites (Fig. 3).

ZVS concentrations ranged from 0.01 % to 0.77 % across all sites, with

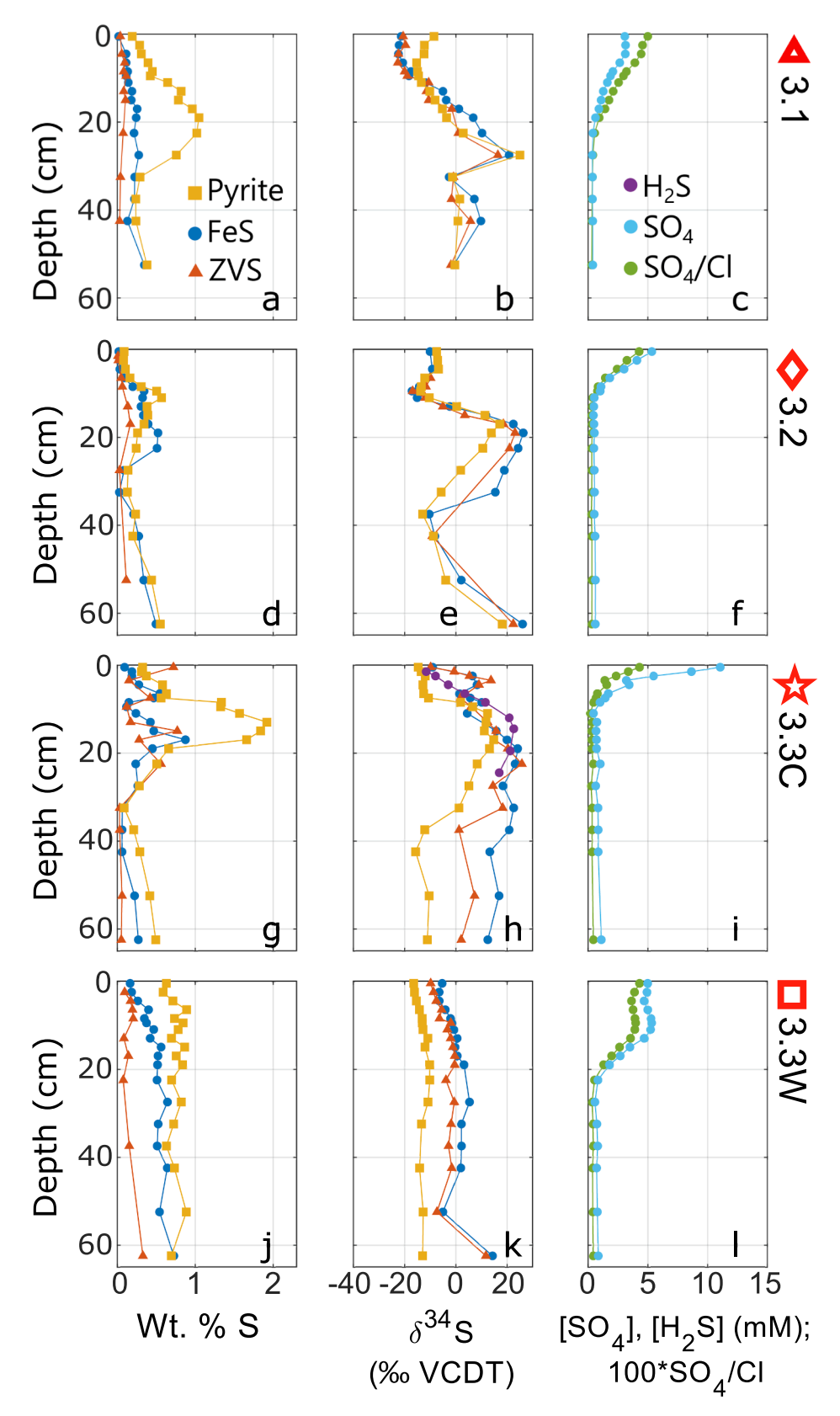


Fig. 2. Sedimentary depth profiles of sulfur species from collected cores. Left panels depict concentrations of solid phase sulfur species (pyrite, FeS, ZVS); center panels depict δ^{34} S values of pyrite, FeS, ZVS, and H₂S; and right panels depict pore water concentrations of dissolved sulfur species. Panels show 3.1 (a–c), 3.2 (d–f), 3.3C (g–i), 3.3W (j–l), 4.3C (m–o), 4.3W (p–r), 5.1C (s–u), 5.1W (v–x), and 5.5 (y–aa).

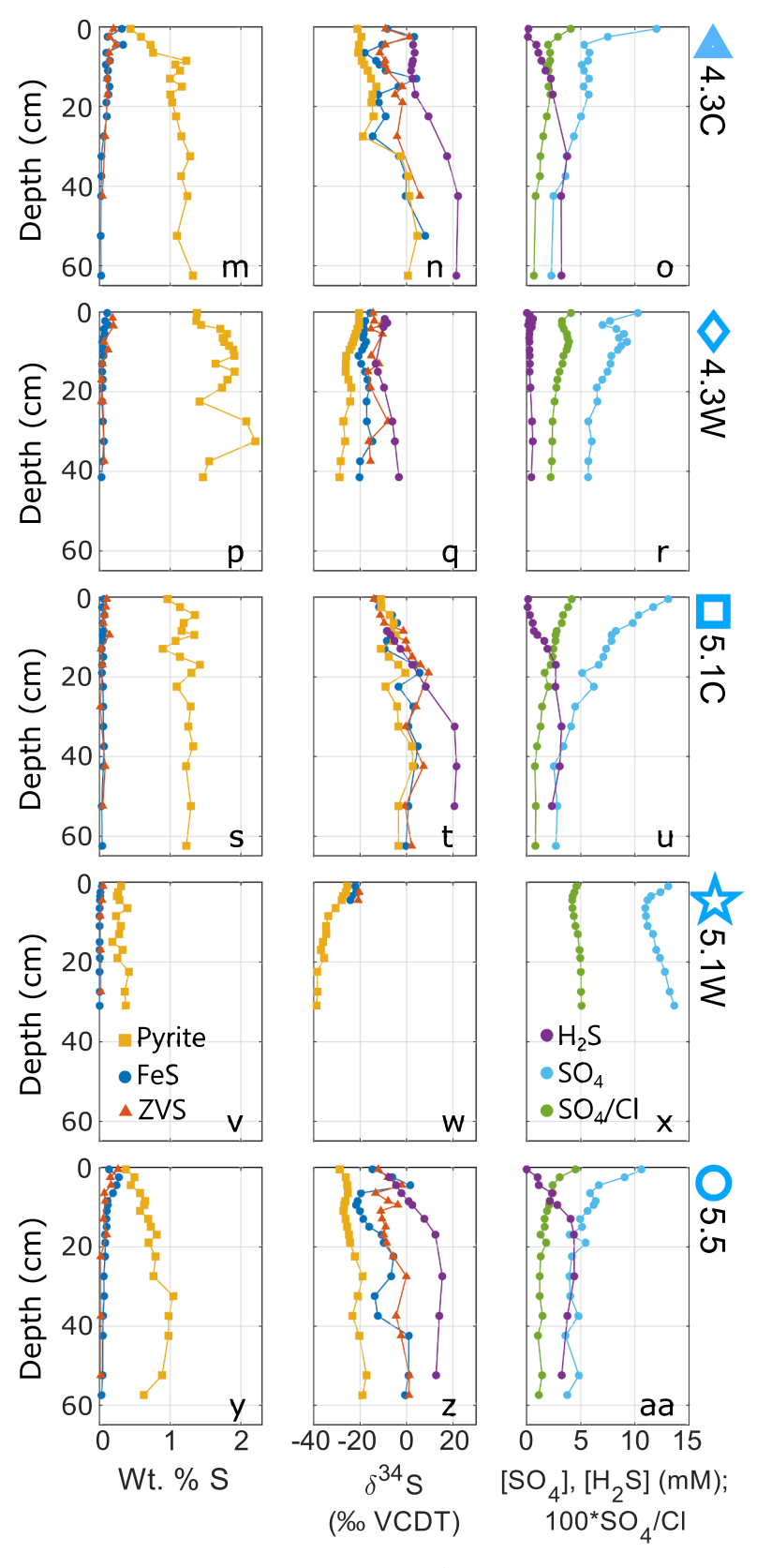


Fig. 2. (continued).

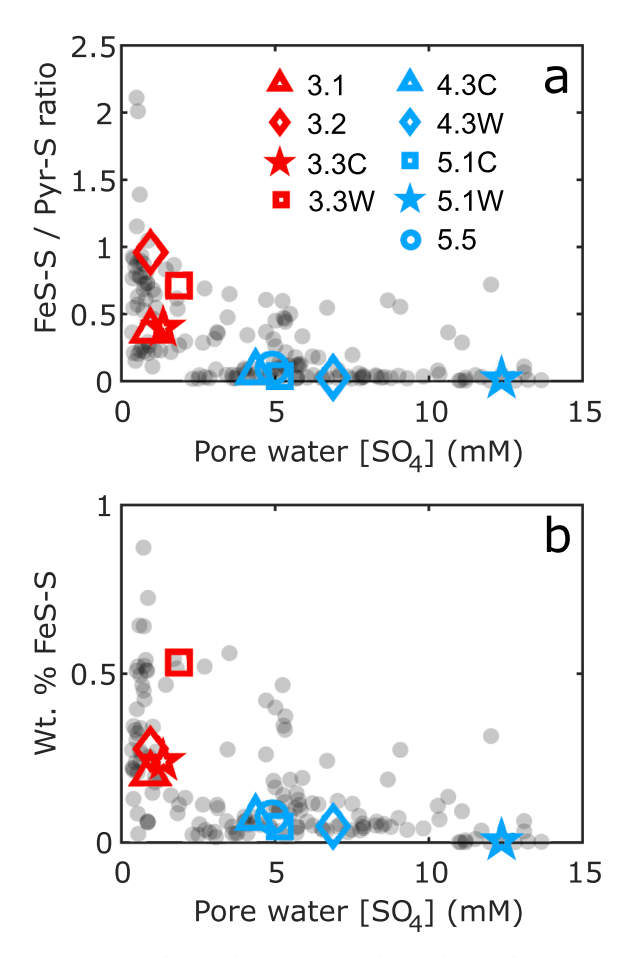


Fig. 3. (a) Ratios of dry weight percent FeS sulfur to dry weight percent pyrite sulfur as a function of pore water sulfate concentration. (b) Dry weight percent FeS sulfur as a function of pore water sulfate concentration. Colored symbols refer to mean values for each sediment core.

the highest mean concentrations found at sites 3.3C and 3.3W. ZVS concentrations decreased downcore at sites 4.3C, 5.1W, and 5.5; attained midcore minima at sites 4.3W and 5.1C; and attained mid-core maxima at sites 3.1, 3.2, and 3.3W (Fig. 2). Site 3.3C featured an unusual ZVS depth profile with very high and variable ZVS concentrations above 25 cm giving way to low and stable concentrations below 25 cm. There were no clear trends in mean ZVS concentration per core as a function of salinity, water depth, or latitude.

Pore water sulfate concentrations and sulfate-to-chloride (SO₄/Cl) ratios generally declined with sediment depth (Fig. 2). These decreases were monotonic or nearly monotonic in six of the nine cores; the exceptions were the three western shoal sites (3.3W, 4.3W, and 5.1W), where initial decreases of [SO₄] in the top 10 cm of sediment gave way to deeper [SO₄] maxima. Sulfate concentrations at the four northernmost sites declined below 1 mM within the upper 25 cm of sediment, while concentrations at the bottoms of the other five cores ranged between 2.3 and 13.7 mM. Similarly, the four northern sites were the only sites at which SO₄/Cl values declined below 10 % of their starting value of 0.051 within the top 30 cm. The shape of each core's SO₄/Cl depth profile tracked with the SO₄ depth profile of that core. Chloride is a conservative tracer that is affected by the physical processes of diffusion, advection, and freshwater-seawater mixing, but not by biochemical reactions. Sulfate is affected by transport and mixing processes, but it is also subject to reactions such as sulfate reduction and sulfide oxidation. Therefore, SO₄/Cl ratios can distinguish biochemical sources and sinks of sulfate from physical processes that can also change sulfate concentration. Chloride normalization is a technique that has been used in previous studies of Chesapeake sulfur cycling (Marvin-DiPasquale et al., 2003) and in many other sediments that are subject to seawaterfreshwater mixing and salinity gradients (Jørgensen, 1977; Swider and Mackin, 1989; Antler et al., 2019).

Pore water sulfide concentrations were measured at sites 4.3C, 4.3W, 5.1C, and 5.5 (Fig. 2). At sites 4.3C, 5.1C, and 5.5, pore water sulfide concentrations were relatively low (generally below 200 μ M) in the top 2 cm but increased with depth to maximum concentrations of 3.2–4.4 mM between 25–35 cm before declining again below those depths. In contrast, pore water sulfide concentration at site 4.3W reached a local maximum of 354 μ M in the top 5 cm (corresponding to a local minimum in [SO₄]) and remained relatively low (<600 μ M) through the rest of the core. Mean pore water sulfide concentration at site 4.3W was 414 μ M—substantially lower

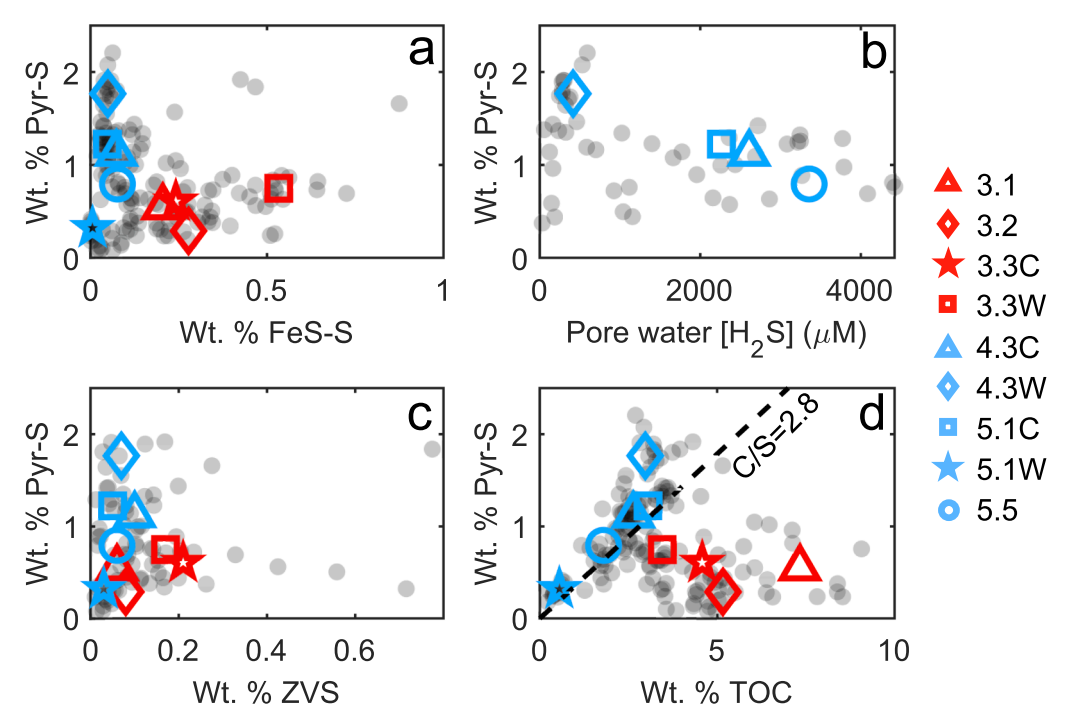


Fig. 4. Weight percent pyrite sulfur as a function of (a) weight percent FeS sulfur, (b) pore water dissolved sulfide concentration, (c) weight percent zero-valent sulfur (ZVS), and (d) weight percent total organic carbon (TOC). Colored symbols refer to mean values for each sediment core. The dashed black line in panel (d) represents a typical marine TOC/pyrite-S ratio of 2.8.

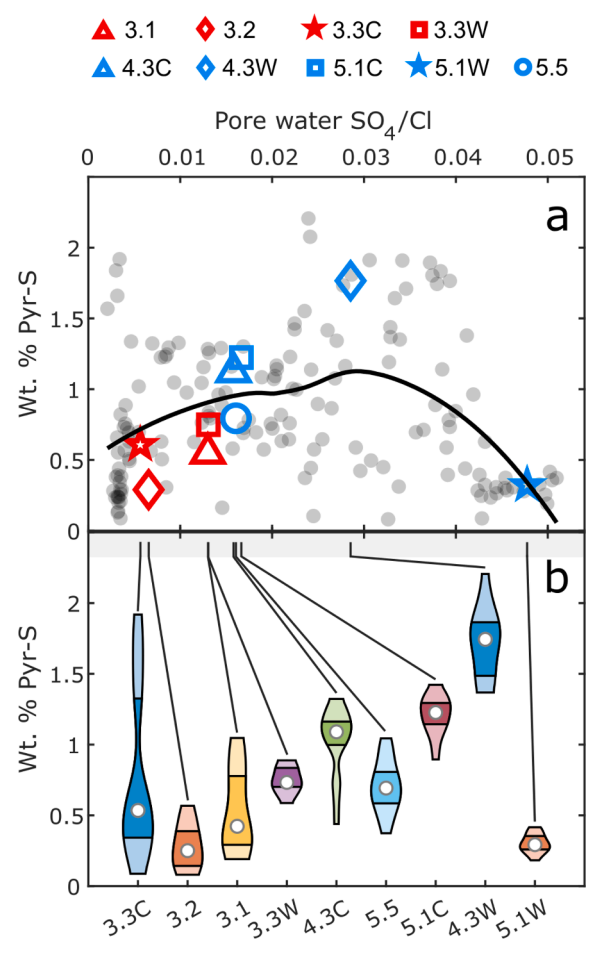


Fig. 5. Weight percent pyrite sulfur versus pore water SO_4/Cl ratios. (a) Gray points refer to individual samples, colored symbols refer to core averages (weighted by sample thicknesses), and the black line is a LOESS regression with a span of 0.7. (b) Violin plots of the distributions of pyrite concentrations in each core. Tops and bottoms of violin plots represent the full range of pyrite concentrations in each core; lines inside each violin represent the upper and lower quartiles; white points inside each violin represent the median. Violin plots are arranged in order of their mean SO_4/Cl ratios. Lines extending from the top of each violin plot indicate that core's mean SO_4/Cl value in the shaded area at the top of panel B, which has the same x-scale as panel A.

than the three other measured sites, whose mean concentrations were between 2.0 and 3.5 mM.

The full set of pyrite concentration values compiled from all cores showed weak correlations to concentrations of AVS (p = 0.12, r = -0.12, n = 159), ZVS (p = 0.50, r = 0.08, n = 79), and TOC (p = 0.19, r = -0.10, n = 158). Correlation of pyrite concentration with H₂S concentration in the southern cores was more significant, but negative (p = 0.01, r = -0.36, n = 50) (Fig. 4). Despite similarly weak linear correlations to [SO₄] (p = 0.11, r = 0.13, n = 155) and SO₄/Cl (p = 0.98, r = -0.002, n = 155), there was a peak in pyrite concentrations in the mid-ranges of SO₄ concentrations and SO₄/Cl ratios (Fig. 5). In contrast, FeS concentrations were maximized under the lowest [SO₄] and SO₄/Cl values. Ratios of FeS to pyrite were higher at the northern sites (3.1, 3.2, 3.3C, and 3.3W) than at the southern sites (4.3C, 4.3W, 5.1C, 51.W, and 5.5; Fig. 4a).

3.2. Sulfur species isotopic compositions

Pyrite $\delta^{34}S$ compositions ranged from -38.7 % to 25.0 % across all cores, FeS $\delta^{34}S$ values ranged from -24.2 % to 26.3 %, ZVS $\delta^{34}S$ values ranged from -22.7 % to 25.8 %, and H_2S $\delta^{34}S$ values ranged from -13.3 % to 22.7 %. The lowest $\delta^{34}S_{pyr}$ values in the data set came from the deeper (>5 cm) samples in core 5.1W, which lacked sufficient FeS and ZVS for $\delta^{34}S$

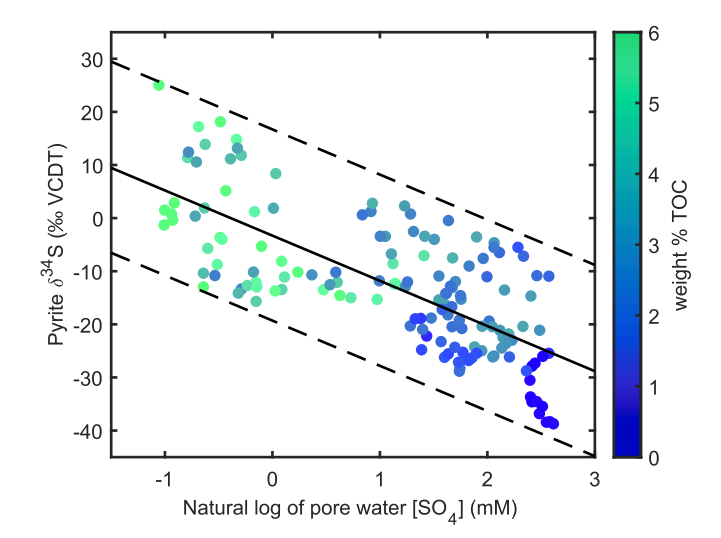


Fig. 6. Pyrite sulfur $\delta^{34}S$ values as a function of the natural logarithm of pore water sulfate concentration ($r^2=0.52$). Colors correspond to TOC concentration. The solid black line is the line of best fit, with the equation y=-8.4ln ([SO₄]) -3.4. The two dashed black lines are parallel to the line of best fit and run 20 % above it and 16 % below it.

measurements of those phases. Depth profiles of pyrite $\delta^{34}S$ values were more variable at sites 3.1, 3.2, 3.3C, and 4.3C than at the other sites. In particular, sites 3.1, 3.2, and 3.3C contained distinctive peaks in pyrite $\delta^{34}S$ values between 10 and 30 cm depth, including one sample of 'superheavy' pyrite (27.5 cm depth at site 3.1) whose $\delta^{34}S$ value exceeded that of modern seawater sulfate.

Notably, pyrite $\delta^{34}S$ values compiled from all cores revealed a logarithmic relationship with pore water SO_4 concentration (Fig. 6). Compiled pyrite $\delta^{34}S$ values from all cores had positive correlations with $\delta^{34}S$ values of FeS (p < 0.0001, r = 0.79, n = 142), ZVS (p < 0.0001, r = 0.76, n = 118), and H_2S (p < 0.0001, r = 0.64, n = 47). Pyrite $\delta^{34}S$ values were mostly lower than those of pyrite's coexisting precursor compounds: the median offset was -6.3 % relative to FeS, -8.8 % relative to ZVS, and -18.7 % relative to H_2S . The $\delta^{34}S_{ZVS}$ – $\delta^{34}S_{pyr}$ and $\delta^{34}S_{H2S}$ – $\delta^{34}S_{pyr}$ offsets reached maxima in the midrange of SO_4/Cl values (Fig. 7).

3.3. TOC abundance and isotopic composition

Organic carbon abundance ranged from 0.2 % to 9.1 %. TOC abundance broadly increased downcore at sites 3.1, 3.2, 3.3C, 3.3W, 5.1C, and 5.5, but remained steady or decreased with depth at 4.3C, 4.3W, and 5.1W (Fig. S1). The δ^{13} C values of TOC ranged from -22.9 % to -27.9 % and core-average δ^{13} C values broadly increased with salinity and with distance from the Susquehanna River mouth (Table 2), in agreement with previous studies (Zimmerman and Canuel, 2001).

3.4. Radiotracer profiles

Radiotracer profiles were obtained for cores 3.1, 3.2, 3.3C, and 5.5. Sedimentation rates calculated from $^{210}\mathrm{Pb}$ and $^{137}\mathrm{Cs}$ analyses are reported in Table 2 and complete depth profile data are included in Table S1. At site 3.1, calculated sedimentation rates were 0.11 cm yr $^{-1}$ ($^{210}\mathrm{Pb}$) and 0.15 cm yr $^{-1}$ ($^{137}\mathrm{Cs}$). At site 3.2, sedimentation rates were 0.33–0.42 cm yr $^{-1}$ ($^{210}\mathrm{Pb}$) and 0.43 cm yr $^{-1}$ ($^{137}\mathrm{Cs}$). At site 3.3C, sedimentation rates were 0.04 cm yr $^{-1}$ ($^{210}\mathrm{Pb}$) and 0.43 cm yr $^{-1}$ ($^{137}\mathrm{Cs}$). At site 5.5, sedimentation rates were 0.27 cm yr $^{-1}$ ($^{210}\mathrm{Pb}$) and 0.40 cm yr $^{-1}$ ($^{137}\mathrm{Cs}$). In the Discussion, we augment these values with sedimentation rates for other core sites drawn from the literature (Colman et al., 2002; Cronin et al., 2003; Hantsoo et al., 2023) as described in the Supplementary Material.

Regression fits used in the CFCS model were significant for three out of four cores, but 210 Pb activities at site 3.2 varied throughout the core and the CFCS model could not be applied to that depth profile. Instead, a minimum

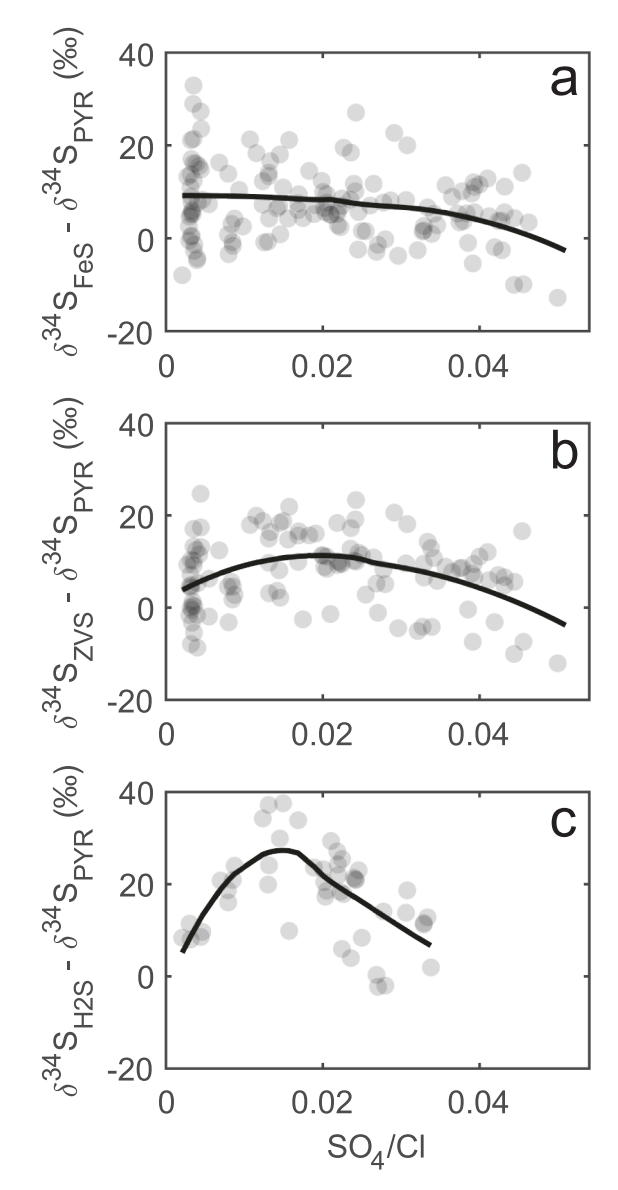


Fig. 7. (a) The offsets between FeS δ^{34} S values and pyrite δ^{34} S values in individual samples. (b) The offsets between zero-valent sulfur (ZVS) δ^{34} S values and pyrite δ^{34} S values in individual samples. (c) The offsets between dissolved sulfide (H₂S) δ^{34} S values and pyrite δ^{34} S values in individual samples. The solid black line in each panel is a LOESS regression with a span of 0.7.

sedimentation rate was calculated by noting the presence of excess ^{210}Pb at a depth of 33 cm. Assuming that ^{210}Pb can be detected for 4–5 half-lives, or $\sim\!100$ yr, the minimum sedimentation rate at site 3.2 should be 0.33 cm yr $^{-1}$. By the same argument, because excess ^{210}Pb was not present at 42 cm depth, the maximum sedimentation rate at site 3.2 should be 0.42 cm yr $^{-1}$. Site 3.2 is located between sites Lee2 and Lee2.5 sampled by Russ and Palinkas (2020). Site Lee2 also has variable ^{210}Pb activities; the minimum ^{210}Pb -derived sedimentation rate at that site is > 0.8 cm yr $^{-1}$ and the ^{137}Cs -derived rate is 0.85 cm yr $^{-1}$. At Lee2.5, both the ^{210}Pb and ^{137}Cs rates are 0.30 cm yr $^{-1}$.

Cesium-based sedimentation rates were higher than lead-based rates for all measured cores, with the largest discrepancy at 3.3C. Measured sedimentation rates generally decrease as the time span over which they are averaged increases (Sadler, 1981). In the northern Chesapeake Bay, sedimentation rate measurements typically differ between the two methods by $\sim\!20$ % with a maximum difference of $\sim\!60$ % (Russ and Palinkas, 2020). The precise causes of this difference are uncertain, though it has been hypothesized that higher cesium-derived sedimentation rates could

potentially result from downward migration of the Cs-137 peak caused by partial desorption of Cs-137 in some sediments (Nittrouer et al., 1984). In the present study, rates differed by $\sim\!20\text{--}30$ %, except at site 3.3C, where the $^{210}\text{Pb}\text{-}\text{based}$ sedimentation rate (0.04 cm yr^-1) was an order of magnitude lower than the $^{137}\text{Cs}\text{-}\text{based}$ sedimentation rate (0.43 cm yr^-1). This may be an artifact of an incomplete ^{210}Pb profile. Site 3.3C is near site LeeS2, where the ^{210}Pb and ^{137}Cs rates are 0.26 cm yr^-1 and 0.29 cm yr^-1, respectively (Russ and Palinkas, 2020), suggesting that the ^{210}Pb sedimentation rate for 3.3C is underestimated and that the ^{137}Cs rate may be the more accurate measurement at that site.

4. Discussion

4.1. Trends in pyrite accumulation and the role of bioturbation

We start by comparing the sedimentary sulfur geochemical trends to SO₄/Cl ratios because SO₄/Cl ratios are responsive to a range of factors such as bioturbation, total organic carbon (TOC) abundance, sedimentation rate, and grain size, all of which influence the degree of sedimentary system openness with respect to sulfate, which plays a major role in sedimentary sulfur geochemistry (Jørgensen, 1979; Halevy et al., 2023). While bioturbation is not the only process that affects SO₄/Cl ratios, mean SO₄/Cl ratios in the Chesapeake Bay cores are positively correlated with mixed layer depth (Fig. 8; Fig. S2), which is a value that can be compared with the geological record of mixed layer depth evolution (Tarhan et al., 2015). The exception to the SO₄/Cl-mixed layer depth trend is site 3.2, which may have been subject to physical reworking (more detailed evaluations of mixed layer depths are presented in the Supplementary Material, including references to Cornwell et al., 1996; Kerhin et al., 1998; Nie et al., 2001). Along with the influence of mixed layer depth on system openness (Fig. 8), we consider a range of biogeochemical factors including reactive iron availability, TOC abundance, sedimentation rate, grain size, and pyrite formation near the sulfate-methane transition zone in our analysis of pyrite burial trends in sediments underlying oxygen-depleted waters.

Pyrite concentrations in the analyzed cores are greatest at intermediate pore water SO₄/Cl values (Fig. 5), while ratios of FeS sulfur to pyrite sulfur are maximized under the lowest SO₄/Cl ratios (Fig. 3). Even if all FeS and ZVS were converted into pyrite, there would still be a peak in the mid-range of SO₄/Cl ratios (Fig. S3). Plotting maximum pyrite concentrations of each core versus the mean SO₄/Cl (Fig. S4) yields a very similar trend to what is seen in Fig. 5; the only substantial difference is in core 3.3C, which has elevated pyrite concentrations at the depth where sulfate is almost completely consumed (8-18 cm) likely due to pyrite formation near the sulfate-methane transition zone. Pyrite $\delta^{34}S$ data also demonstrate that sedimentary sulfur cycling is impacted the degree of system openness, similar to other marine sediments (Jørgensen, 1979; Lyons et al., 2003; Masterson et al., 2018; Pasquier et al., 2021; Halevy et al., 2023). Pyrite δ^{34} S values are elevated at low pore water sulfate concentrations (Fig. 6) because a low degree of system openness results in evolution of sedimentary sulfide $\delta^{34}S$ values to higher values. Pyrite is ^{34}S -depleted at the high end of pore water sulfate concentrations, reflecting open system conditions that enable low δ^{34} S values to be preserved (Jørgensen, 1979).

Core averages and a LOESS regression fit to data from across all cores indicate that pyrite concentrations peak near a SO_4/Cl ratio of 0.03, roughly intermediate between zero and the modern seawater value of 0.051 (Fig. 5). These data imply that rapid sulfate depletion in organic-rich, non-bioturbated sediments that have low SO_4/Cl ratios may limit pyrite accumulation. On the other end, enhanced transport of oxidants into permeable or heavily bioturbated sediments with high SO_4/Cl ratios suppresses pyrite formation and retention. Intermediate SO_4/Cl ratios are found in sediments where mild bioturbation and/or sulfide oxidizing bacteria that thrive in sediments with mild bioturbation (Malkin et al., 2022) promote the transport or production of sufficient oxidants to give rise to mixed-valence sulfur species that generate polysulfides, thus promoting pyrite formation (Rickard, 1975; Hantsoo et al., 2023).

The SO₄/Cl ratio reflects the balance between the sources and sinks of pore water sulfate which are also impacted by sedimentation rate, grain

Table 2
Mean sulfur and carbon data for the collected cores, along with radiotracer-based sedimentation rates. All means are weighted by the stratigraphic thicknesses of sediment samples.

		3.1	3.2	3.3C	3.3W	4.3C	4.3W	5.1C	5.1W	5.5
Sedimentation rate	²¹⁰ Pb	0.11	0.33-0.42	0.04						0.27
	(cm yr ⁻¹)									
	¹³⁷ Cs	0.15	0.43	0.43						0.40
	(cm yr ⁻¹)									
Mean species concentration	SO ₄ (mM)	0.94	0.95	1.36	1.87	4.36	6.89	5.15	12.36	4.91
1	100 * SO ₄ /Cl	1.30	0.66	0.56	1.31	1.58	2.85	1.66	4.78	1.61
	Pyrite (wt. %)	0.55	0.29	0.61	0.75	1.12	1.77	1.22	0.32	0.79
	FeS (wt. %)	0.20	0.28	0.24	0.53	0.07	0.05	0.05	0.01	0.08
	ZVS (wt. %)	0.06	0.08	0.21	0.17	0.10	0.07	0.05	0.03	0.06
	H ₂ S (mM)					2.6	0.4	2.3		3.4
	TOC (wt. %)	7.33	5.16	4.57	3.45	2.63	2.97	3.05	0.55	1.79
Mean isotopic composition	Pyrite (‰ VCDT)	-0.4	0.0	-2.1	-12.5	-8.0	-25.7	-3.8	-34.9	-22.2
	FeS (% VCDT)	1.6	6.6	16.1	1.9	-4.7	-17.9	-0.4	-22.7	-8.5
	ZVS (‰ VCDT)	-2.3	6.7	11.1	-1.6	-3.0	-13.6	1.1	-20.6	-4.5
	H ₂ S (‰ VCDT)			12.9		12.7	-7.2	11.8		10.1
	TOC (‰ VPDB)	-25.4	-26.1	-25.2	-25.9	-25.5	-24.8	-24.2	-25.8	-24.1

size, TOC abundance, and bioturbation. These factors are expressed in the advection–diffusion-reaction equation (Arndt et al., 2013) that is used to model sedimentary sulfur cycling and biogeochemistry (Jørgensen, 1979; Masterson et al., 2018). Our use of SO_4/Cl ratios is conceptually similar to the well-established use of sulfate-methane transition depths and shapes of sulfate depth profiles to assess the strengths of different sources and sinks of sulfate through a sediment column (Boudreau and Westrich, 1984; Borowski et al., 1999; Jørgensen et al., 2024). In other words, the mean SO_4 concentration of a sediment column down to an arbitrary depth is essentially a function of the mixed layer depth, the shape of the concentration curve below the mixed layer, and the depth of sulfate depletion. Because our cores were not deep enough to consistently capture the interval of full sulfate depletion in all cores, we instead use the mean SO_4/Cl values of our cores for the same purpose.

4.1.1. Assessing Fe limitation in Chesapeake Bay sediments

Previously published Fe geochemistry from Chesapeake Bay indicates that the observed relationship between SO₄/Cl values and pyrite abundance is unlikely to be strongly influenced by Fe limitation in the collected cores. Pyrite formation is less likely to be Fe-limited in sediments that contain appreciable FeS because no new Fe is needed for FeS to form pyrite (Eqs. (1) and (2)). Therefore, high concentrations of FeS at the four northern sites (0.2-0.5 %, on average; Table 2) indicate that pyrite formation is less likely to be Fe-limited in that part of the Bay. High amounts of HCl-soluble Fe in the mid-to-northern Bay (200–400 μmol g⁻¹; Cornwell and Sampou, 1995) also indicate that iron is available for pyrite formation at these sites. In contrast, an excess of aqueous sulfide could indicate that pyrite formation is limited by Fe. Thus, the sites most likely to be Fe-limited are those with both low FeS/pyrite ratios and abundant pore water H₂S: specifically, sites 4.3C, 4.3W, 5.1C, and 5.5. Three of these sites (4.3C, 4.3W, and 5.1C), have the highest mean pyrite concentrations of all the studied sites.

One means of assessing Fe limitation in the sites with excess pore water sulfide is the degree of pyritization (DOP), i.e. the fraction of reactive Fe (pyrite Fe plus HCl-soluble Fe) that has been converted into pyrite (Raiswell et al., 2018). Near sites 4.3C and 4.3W, the DOP of sediments post-dating the onset of eutrophication (ca. 1800 CE) ranges between $\sim\!0.25$ and 0.60, with most samples falling below 0.45 (Cooper and Brush, 1991). In the mid-to-southern Bay (closer to sites 5.1C and 5.5), DOP values from the top 20 cm of sediments also range between 0.25 and 0.60, while oxalate-extractable Fe concentrations (a subset of the highly reactive Fe pool) are in the range of 25–100 $\mu mol\ g^{-1}$ (Cornwell and Sampou, 1995). This may be compared to another hypoxic basin, the Bornholm Basin of the Baltic Sea, in which mild to moderate Fe limitation is posited for sediments with total non-sulfur-bound reactive Fe concentrations of 7–25 $\mu mol\ g^{-1}$

(Liu et al., 2021). It should be noted, however, that a large range of DOP values (0.45–0.8) could potentially indicate Fe limitation if water column redox conditions are highly variable, and that Fe limitation proxies can be difficult to interpret in systems subject to such fluctuations (Raiswell et al., 2018). Therefore, while available DOP data do not imply that pyrite formation is Fe-limited at these sites, further geochemical constraints on Fe mineralogy may allow more conclusive characterization of Chesapeake Bay sedimentary Fe cycling.

Additional geochemical data in mid-Bay sediments indicate the presence of highly reactive Fe at depth near sites 4.3C and 4.3W. Spectroscopic analyses of mid-Bay sediments near these sites show that sulfide-reactive Fe (II) and Fe(III) minerals (lepidocrocite, vivianite, nikischerite) persist in appreciable concentrations to > 30 cm depth (Li et al., 2015), even though these sediments contain dissolved sulfide for at least part of the year (Fig. 2). The co-occurrence of reactive Fe with dissolved sulfide is unusual but not without precedent; for example, sediments of the hypoxic Santa Barbara basin retain both reactive Fe-oxides and dissolved sulfide over time scales of ~100 yr, which may occur because high sedimentation rates (0.4 cm yr⁻¹) shorten the duration of Fe(III) interaction with pore water sulfide in that basin (Wang et al., 2019). Organic carbon may also preserve Fe(III) minerals in sediments, as the complexation of Fe(III) with organic matter slows the rate of Fe-oxide sulfidation and pyrite formation (Morse and Wang, 1997; ThomasArrigo et al., 2020); this has been suggested as an explanation for the persistence of Fe(III) to depth in sediments containing 2-5 % TOC under hypoxic water (Figueroa et al., 2023). However, these mechanisms still do not explain the persistence of sulfide-soluble Fe(II) minerals such as vivianite in deeper mid-Bay sediments. We suggest that this may result from seasonal oscillations in the dissolved sulfide concentration of mid-Bay pore waters, which can drop to near-zero values in winter and spring (Roden and Tuttle, 1993; Malkin et al., 2022). This may occur in concert with Fe-based anaerobic oxidation of methane (AOM), which converts reactive iron oxides to Fe^{2+} (Egger et al., 2014). In light of the data presented by Li et al. (2015), we consider Fe limitation unlikely at sites 4.3C and 4.3W. Mild Fe limitation remains a possibility at sites 5.1C and 5.5 in light of uncertainties in interpreting DOP data, but we do not expect that this would fundamentally alter our interpretation of the SO₄/ Cl-pyrite trend shown in Fig. 5. Fe cycling is difficult to characterize under the variable water column redox conditions and mixed TOC sources that typify the Chesapeake Bay, but we find that SO₄/Cl ratios can provide a useful integrated signal of sedimentary system openness and sulfur redox cycling.

4.1.2. Spatial trends and pathways of Chesapeake pyrite formation

In normal marine sediments, pyrite concentration typically scales with the concentration of TOC because the degradation of organic matter

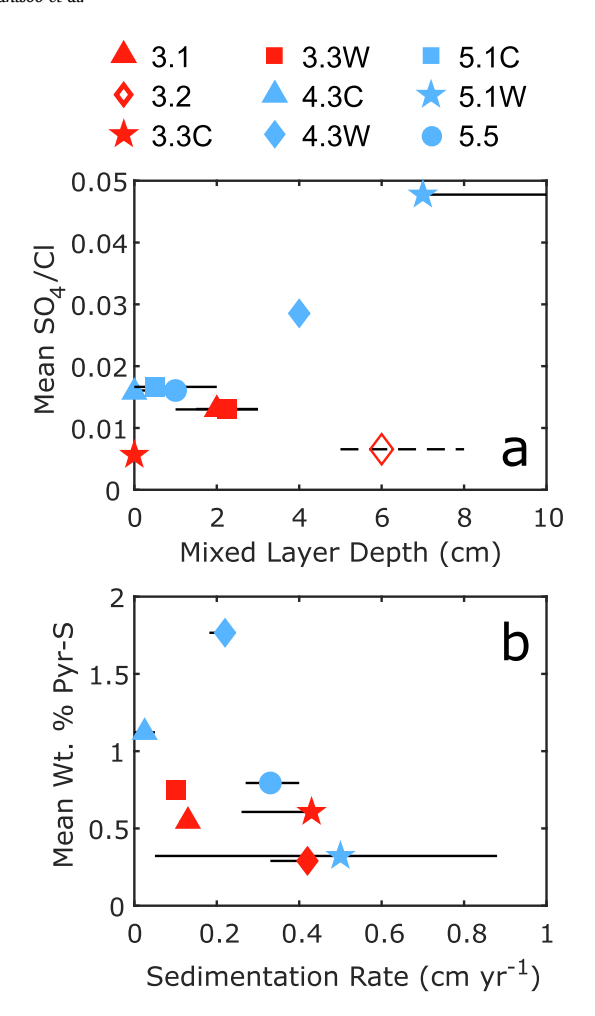


Fig. 8. (a) Mean SO_4/Cl ratio of each core plotted against the estimated mixed layer depth of each core, as described in the Supplementary Material. Horizontal bars represent potential ranges of mixed layer depths. The unfilled marker and dashed bar for Site 3.2 indicate that its mixed layer depth may result from physical reworking. (b) Mean pyrite sulfur concentration of each core plotted against the estimated sedimentation rate of each core. Sedimentation rates that were not calculated in this study are described in the Supplementary Material.

consumes oxygen (and other oxidants) and ultimately fuels sulfate reduction (Berner, 1984). In the Chesapeake Bay, pyrite accumulation under intermediate SO₄/Cl values is not an artifact of higher TOC concentrations in that range. Instead, higher TOC concentrations are associated with low SO₄/Cl ratios, which is consistent with the idea that elevated TOC concentrations promote sulfate drawdown. Despite high variability, pyrite-S/ TOC ratios decrease sharply when SO₄/Cl ratios drop below ~0.02 (Fig. S5). Conversely, FeS-S/pyrite-S ratios increase sharply as sulfate concentrations decrease below ~3 mM, particularly in the northern cores (Fig. 3, Fig. S6). Therefore, we suggest that pyrite accumulation in the most reducing sediments of the Chesapeake Bay is inhibited in part by a lack of intermediate redox species of sulfur. Our data suggest that in strongly reducing, sulfate-depleted sediments, FeS is much more likely to accumulate in the upper ~ 1 m of sediment without being converted to pyrite. If pore waters become more acidic with depth, it is likely that some of the FeS will later be converted to pyrite via the H₂S pathway as a fraction of the existing FeS dissolves and releases sulfide back into solution (Rickard, 2012). However, even if all of the existing FeS and ZVS in these samples were converted into pyrite sulfur, there would still be a maximum of pyrite concentration in the mid-range of SO₄/Cl ratios (Fig. S3). This implies that there is some other factor beyond the slow pyritization of FeS that limits the amount of pyrite that can form in strongly reducing sediments.

Inhibited conversion of FeS to pyrite due to pore water sulfate depletion

has previously been posited for low-salinity sediments of the northern Chesapeake Bay (Berner et al., 1979) and for Pleistocene Black Sea sediments deposited under low salinity (Berner, 1974). High FeS-S/pyrite-S ratios also persist under higher but more variable salinities in the eutrophic Peel-Harvey estuary (Western Australia), an effect likewise attributed to slow reaction of FeS with H₂S in strongly reducing pore waters (Kraal et al., 2013; Valesini et al., 2019). In the hypoxic to euxinic Kau Bay (Indonesia), FeS remains stable throughout the Holocene marine layer despite near-marine salinity; lack of oxidizing power is similarly proposed to explain this feature (Middelburg, 1991). In sediments underlying the anoxic brine of the Orca Basin (Gulf of Mexico), spatial separation between FeS and ZVS along with low rates of sulfate reduction are proposed as dual causes of high FeS-S/pyrite-S ratios (Hurtgen et al., 1999). An alternate hypothesis proposes that very high reactive iron concentrations (HClextractable Fe concentrations of 300–800 µmol g⁻¹) may slow pyrite formation by drawing dissolved sulfide into FeS at the expense of the FeS-H₂S reaction (Gagnon et al., 1995). Chesapeake Bay sediments north of sites 4.3C and 4.3W generally have HCl-extractable Fe concentrations of 150–300 μ mol g⁻¹, though this value can exceed 300 μ mol g⁻¹ north of site 3.2 (Cornwell and Sampou, 1995); therefore, it is possible that Fe scavenging of sulfide also contributes to the high FeS/pyrite ratios at the northernmost study sites.

The data collected from the Chesapeake Bay cores can be used to estimate which of the three experimentally demonstrated pyrite-forming reactions (H₂S, polysulfide, and ferric hydroxide surface) are more or less likely in these sediments. With regard to the ferric hydroxide surface (FHS) pathway, sediments with high terrigenous input under low salinity are more likely to form FHS-derived pyrite because of the high ratio of Fe(III) minerals to H2S in terrestrial systems; therefore, it has been proposed that the FHS pathway is unlikely in sediments with appreciable FeS accumulation because the presence of FeS signals a low Fe(III):H2S ratio (Wan et al., 2017). However, the Chesapeake Bay does not appear to fit this model; our results show that the northern Bay, which bears the highest terrigenous sediment load, the highest reactive Fe fraction, and the lowest salinity, is also the area with the highest sedimentary FeS concentrations. This leads us to conclude that the FHS reaction pathway is probably not a significant source of pyrite in Chesapeake Bay sediments, though it may be important in pyrite nucleation.

Across all sites and all samples, pyrite sulfur isotope systematics broadly adhere to open/closed system dynamics: low concentrations of pore water sulfate and high concentrations of TOC are correlated with higher pyrite $\delta^{34}S$ values (Fig. 6). The influence of system openness on pyrite S isotope trends has been well established by foundational modeling studies (e.g., Jørgensen, 1979) as well as more recent work (e.g., Halevy et al., 2023). However, although the aggregate of all samples fits existing models of sedimentary sulfur geochemistry, subtleties emerge in individual cores. For example, three of the northern cores (3.1, 3.2, and 3.3C) show well defined peaks of pyrite $\delta^{34}S$ values close to the depth of sulfate depletion (Fig. 2, Fig. S7). Stratigraphic peaks in pyrite concentration at sites 3.1, 3.2, and 3.3C occur close to the δ^{34} S peaks and likely result from pyrite formation near the sulfate-methane transition (SMT) zone via the H₂S pyrite formation pathway (Fig. S8). Pyrite formation near the SMT has been shown to result in the formation of ³⁴S-enriched pyrite (Liu et al., 2021). A peak in pyrite concentrations and $\delta^{34}\text{S}$ values could also result from transient increases in sediment deposition or increases in the amount or lability of organic carbon. Assuming linear sedimentation rates of 0.13, 0.42, and 0.43 cm yr⁻¹ for 3.1, 3.2, and 3.3C respectively, the δ^{34} S peaks at these sites occur in sediments dating to 1807 CE, 1979 CE, and 1979 CE. This raises the possibility that a storm event within the last ~40 yr may have caused transient changes in sedimentation rate or TOC concentrations at sites 3.2 and 3.3C. However, we do not observe large changes in TOC concentrations at these depths (Fig. S1) at site 3.2 or 3.3C, nor do we note sediment characteristics that would suggest storm deposition at or above these depths. Instead, it is likely that oxygen depletion resulting from enhanced nutrient runoff from the Susquehanna River (Brush, 2001) led to the development of an SMT that enhanced pyrite formation at these depths (Thiel et al., 2019). On the other hand, site 3.1 does bear a peak in TOC

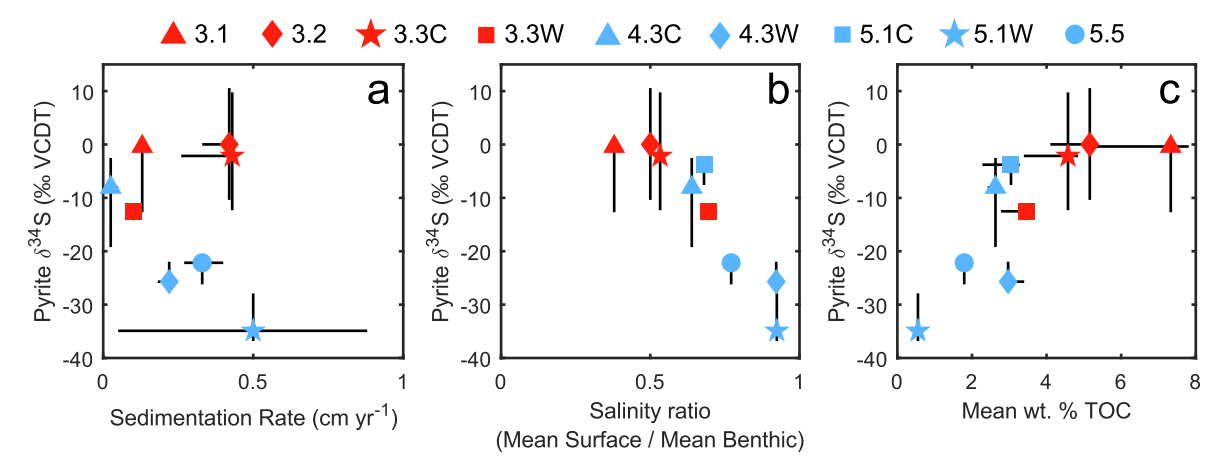


Fig. 9. (a) Mean pyrite sulfur δ^{34} S value of each core plotted against sedimentation rate of each core. Vertical bars represent 1st and 3rd quartiles for each core; horizontal bars represent possible ranges of sedimentation rates. (b) Mean pyrite sulfur δ^{34} S value of each core plotted against that site's ratio of mean annual surface salinity to mean annual benthic salinity, as determined from monitoring data from 1984 to 2017 (Table 1). Vertical bars are as in panel a. (c) Mean pyrite sulfur δ^{34} S value of each core plotted against mean TOC concentration of each core. Horizontal bars represent 1st and 3rd quartiles of TOC concentration for each core; vertical bars are as in panel a.

concentration at the same depth as its pyrite δ^{34} S peak, implying that sedimentary organic carbon supply may have influenced pyrite isotopic evolution in addition to changing water column conditions over the last two centuries.

The sulfur cycling of SMT and sub-SMT sediments can be complex, particularly in very shallow SMT zones; sediments can retain sufficient oxidizing power in the reactive iron pool and/or in elemental sulfur to continue generating polysulfides within or below the SMT (Holmkvist et al., 2011), and polysulfide compounds have been found in close association with anaerobic oxidation of methane (Milucka et al., 2012). Sites 3.2 and 3.3C retain relatively high amounts of ZVS just below the SMT, and this ZVS has a similar isotopic composition to pyrite and FeS in the zones of maximum pyrite concentration, suggesting a possible role for the polysulfide pathway even in SMT sediments. Nevertheless, the peaks in $\delta^{34} S_{pyr}$ values in association with increases in pyrite concentration near the SMT imply that the H_2S pathway is more significant at the northern sites than at the southern sites—particularly at sites 3.1, 3.2, and 3.3C—but the buildup of FeS in northern sediments also implies that the H_2S pathway might be less efficient than the polysulfide pathway in the Chesapeake Bay.

Paired pyrite concentration and pyrite δ³⁴S data suggest that the H₂S reaction pathway is more significant at three northern sites (3.1, 3.2, 3.3C) that have low mean SO₄/Cl ratios. At other sites with more intermediate SO₄/Cl ratios, it is likely that the polysulfide reaction pathway is more prominent in early pyrite formation near the sediment-water interface. The δ^{34} S offset between ZVS and pyrite reaches a LOESS-fit maximum of $\sim 11 \%$ under intermediate SO₄/Cl ratios, which is much smaller than the ~30 % offset between H₂S and pyrite in the same range (Fig. 7). The large gap between δ^{34} S values of pyrite and H₂S in this interval implies either that pyrite is not precipitating in this SO₄/Cl range, or that pyrite is mostly precipitating via the polysulfide pathway. Determining the sources of pyrite sulfur from the δ^{34} S values of its reactant compounds is difficult because the more labile precursor species can evolve separately from the accumulating product pyrite, particularly as sediment depth increases (Raven et al., 2016). However, pyrite δ^{34} S values that are anomalously lower than those of all coexisting pyrite precursor species (FeS, ZVS, and H₂S) have been noted in many modern settings, including in very shallow sediments (Kaplan et al., 1963; Raven et al., 2016; Strauss et al., 2012; Zopfi et al., 2008; Gomes et al., 2022; Hantsoo et al., 2023). In most of our cores (3.3C, 3.3W, 4.3C, 4.3W, 5.1W, and 5.5), pyrite δ^{34} S values are lower than those of all measured coexisting precursor compounds at nearly all depths. It is difficult to resolve an apparent isotopic mass imbalance that persists through nearly every sample in a sediment core, but one mechanism that can partially bridge this isotopic gap is rapid internal fractionation in the polysulfide pool (Amrani et al., 2006), which can cause ZVS δ^{34} S values to exceed 'instantaneous' product pyrite δ^{34} S values by up to 7

% (Hantsoo et al., 2023). Therefore, in spite of the limitations of tracking labile reactants against a more stable product, it is more parsimonious from a mass balance perspective to reconcile the trends in Fig. 7 with the polysulfide pathway than with the H_2S pathway. While future geomicrobiological studies may provide a more nuanced view of the relative impact of the different pyrite formation pathways in Chesapeake Bay, the sulfur isotope geochemistry of the cores (Fig. 2, Fig. 7) is consistent with early pyrite formation near the sediment—water interface occurring primarily via the polysulfide pathway, with later pyrite formation near the SMT occurring primarily via the H_2S pathway.

Sedimentation rate can strongly influence pyrite sulfur isotope trends because more rapid sediment deposition draws a sediment column toward closed-system conditions and thus toward higher pyrite δ^{34} S values (Claypool, 2004; Pasquier et al., 2017; Liu et al., 2021; Bryant et al., 2023). In spite of this, core-average δ^{34} S values in the Chesapeake Bay do not show a strong correlation to sedimentation rate and may actually be lower at high sedimentation rates (Fig. 9a). Instead, Chesapeake Bay core-average pyrite $\delta^{34}S$ values show much stronger correlations to water column stratification and sedimentary TOC abundance (Fig. 9b-c). This probably occurs because the Chesapeake Bay has much more variability in TOC and water column stratification than more distal sites, where sedimentation rate will exert proportionally more influence on pyrite δ^{34} S evolution (e.g., Pasquier et al., 2021; Bryant et al., 2023). Nevertheless, the northern Chesapeake Bay sites also preserve stratigraphic swings in pyrite δ^{34} S values-likely derived from anthropogenic changes in sedimentation rate and water column oxygen depletion (Brush, 2001)—that are superimposed on their higher mean δ^{34} S profiles. Thus, while sedimentation rate is a critical factor that governs pyrite δ^{34} S values on a global scale, the data from our cores also highlight the influence that strong changes in biogeochemical cycling at low and variable water column oxygen concentrations can exert on sedimentary system openness.

4.1.3. Sulfate supply, sulfate demand, and bioturbation

Diagenetic pyrite accumulation depends on the total sedimentary sulfate reduction flux and on the fraction of sulfide that is retained in sediments. These two parameters can be likened to 'gross sulfate reduction' and 'net sulfate reduction' (Moeslund et al., 1994; Jørgensen, 2021). The microbial sulfate reduction flux in turn depends on the availability of sulfate and organic matter to sulfate reducing microorganisms. Sulfate is supplied to pore water by molecular diffusion from the water column, biodiffusion (i.e., diffusive particle mixing via bioturbation), bioirrigation (i.e., advective fluid flow via bioturbation), sulfide oxidation, and sulfur disproportionation; sulfate is removed from pore water by burial advection (i.e., due to sedimentation) and sulfate reduction (Berner, 1980; Arndt et al., 2013).

Therefore, processes that increase the supply of sulfate and TOC should increase gross sulfate reduction rates. On the other hand, the physical processes that add sulfate to pore waters can also add solutes (i.e., dissolved O2) and solids (i.e., Fe- and Mn-oxides) that partially or fully oxidize sulfides. This implies that greater sulfate supply from molecular diffusion and bioturbation could increase gross sulfate reduction but decrease net sulfate reduction. However, as explored in Section 4.1.2, partial oxidation of dissolved sulfide may actually increase pyrite precipitation by introducing mixed-valence sulfur species that generate polysulfides. We propose that bioturbation can increase shallow sedimentary pyrite precipitation when two conditions are met: first, high microbial sulfate demand must be matched by high sulfate supply to increase gross sulfate reduction rates; second, the sedimentary dissolved sulfur pool must be oxidized enough to promote conversion of FeS to pyrite via polysulfide, but not so oxidized—as in the case of core 5.1W-that little dissolved sulfide can accumulate and pyrite is susceptible to oxidation.

In shallow sediments, low average SO₄/Cl ratios are found when the sum of the depth-integrated sulfate sinks greatly exceeds that of the sulfate sources, i.e. when there is a large deficit of sulfate supply relative to microbial sulfate demand. A sediment column with high sulfate demand and low sulfate supply has some aspects in common with a closed system sediment column. 'Closed system' means that the diffusional sulfate flux into the sediment column is limited or is much smaller than the advective burial flux as a result of high sedimentation rates (Claypool, 2004; Jørgensen et al., 2004). The gap between sulfate demand and sulfate supply tends to increase under high sedimentation rate (which increases the speed with which pore waters are separated from the water column), fine grain size (which slows the downward diffusion of water column sulfate), and high fluxes of labile organic carbon (which can be sourced from the overlying water column or from the underlying methanogenic zone). For example, a strong sulfate deficit is reflected in the rapid decline of pore water sulfate concentration with depth at sites that have high sedimentation rates (e.g., site 3.2) and/or high TOC concentrations (e.g., sites 3.1 and 3.3C). Higher sedimentation rates are broadly correlated with lower pyrite concentrations in the Chesapeake Bay cores (Fig. 8), which may reflect the role of rapid sedimentation in limiting the diffusive supply of sulfate and sequestering reduced sulfur as FeS rather than pyrite. The role of sedimentation rate in pyrite burial is somewhat complex and depends on the diagenetic time scale being considered; faster sedimentation may allocate more labile organic matter toward sulfate reduction, thus increasing early pyrite formation (Berner, 1984), but over longer time scales it may advect reactive Fe species below the sulfidic zone of sediments and limit later pyrite formation (Raiswell, 1993). In either case, rapid sedimentation tends to shift a sediment column toward closed-system conditions with respect to sulfate.

The data from the Chesapeake Bay indicate that non-bioturbated sediments in which sulfate is rapidly depleted may impede shallow pyrite precipitation, while permeable or heavily bioturbated sediments contain enough oxidants to suppress pyrite formation and retention. The result is that pyrite accumulation is broadly maximized in the mid-range of SO₄/Cl ratios (Fig. 5), although there is a notable exception to this trend at 8–18 cm depth in core 3.3C, which appears to result from the production of H₂S derived from anaerobic oxidation of methane and other processes that promote pyrite formation near the SMT (see discussion in section 4.1.2). Shallow SMT depths, low average SO₄/Cl ratios, and the persistence of FeS with depth in the four northern cores all indicate that sulfate demand greatly exceeds sulfate supply at those sites. At the other extreme, site 5.1W has a relatively high sand fraction and low concentrations of TOC, which inhibits sulfate reduction, promotes transport of oxidants that can oxidize dissolved sulfide and pyrite, and yields high SO₄/Cl ratios. The other four southern sites are characterized by more intermediate SO₄/Cl ratios and lower FeS-S/pyrite-S ratios than the northern sites; these features indicate a smaller deficit between sulfate supply and demand.

It is notable that the highest mean pyrite concentration of the nine cores is found at site 4.3W, which has a mixed layer depth of 4 cm and a biodiffusion rate of $5.1~{\rm cm}^2~{\rm yr}^{-1}$ (Hantsoo et al., 2023). Sediments in the vicinity of site 4.3W tend to have higher gross sulfate reduction rates than

sediments farther north or south in the Bay, and microbial sulfate reduction in the vicinity of that site persists at high rates to at least 10 cm depth, even as dissolved sulfide accumulates to millimolar concentrations in the same horizon (Marvin-DiPasquale and Capone, 1998). At 15–20 cm depth, sulfate concentrations near site 4.3W oscillate annually between 4 mM (March–May) and 0 mM (August–September) while dissolved sulfide oscillates between 1 and 4 mM in the same interval (Marvin-DiPasquale et al., 2003). The coexistence of multiple oxidation states of sulfur in concentration ratios that fluctuate seasonally at depths well below the sediment mixed layer may contribute to the high amounts of pyrite at this site, and to its high pyrite/TOC ratios (Fig. 3). This may be relevant to early Paleozoic trends in pyrite accumulation under fluctuating redox conditions (Pruss and Gill, 2024), which we will examine in more detail in Section 4.2.

Pore water SO_4/Cl ratios in shallow Chesapeake Bay sediments are likely to vary seasonally due to differences in sulfate reduction rates (Roden and Tuttle, 1993). We sampled in July–August to capture SO_4/Cl trends during an interval of maximum sulfate depletion; therefore, the relationship between pyrite burial and SO_4/Cl ratios in this data set reflects an interval when sulfate reduction is most active. This time period also corresponds to the time when there is net pyrite precipitation in Chesapeake Bay surface sediments (Hantsoo et al., 2023). Despite this seasonal variability, the correspondence between pyrite concentrations and pore water SO_4/Cl values during an interval of net pyrite precipitation implies that sulfate supply versus demand plays a large role in determining patterns of pyrite burial in systems with low and variable benthic oxygen concentrations.

As noted previously, pyrite accumulation depends not only on the total sedimentary sulfate reduction flux but also on the fraction of sulfide that is retained in sediments. There is strong evidence that bioturbation increases total or 'gross' sulfate reduction rates, yet it has been argued that incipient bioturbation in the early Paleozoic probably decreased pyrite burial because it drove down pore water sulfide retention rates and/or drove up pyrite reoxidation rates (Canfield and Farquhar, 2009; van de Velde et al., 2018). In our estimation, this model of Paleozoic pyrite burial does not take into account the higher sulfate reduction rates that mild bioturbation can stimulate and the role of polysulfide in pyrite precipitation. In Section 4.2, we explore how changes in sulfate demand and in the balance between sulfate reduction and sulfide reoxidation may have affected pyrite deposition in the early Paleozoic Era.

4.2. An alternative model of Paleozoic pyrite burial

Earth system models have assumed that the Paleozoic evolution of bioturbation led to less retention of sulfide in sediments, which led to less marine pyrite burial (Canfield and Farquhar, 2009; Tarhan et al., 2015; van de Velde et al., 2018). Based on the data collected in this study, we propose an alternative hypothesis: early Paleozoic bioturbation temporarily increased global pyrite burial fluxes by (a) increasing sulfide retention and pyrite precipitation rates via partial sulfide oxidation to ZVS species, and/ or (b) increasing sulfate reduction rates by increasing the supply of sulfate and organic matter to sediments. It is likely that this increase in pyrite burial efficiency would not have been a permanent feature. In Section 4.2, we use insights from the geologic record and a global biogeochemical model to evaluate whether pyrite burial efficiency reached a maximum at some point in the Paleozoic, after which the further addition of oxidants to sediments-both through greater ocean-atmosphere pO2 and through intensifying rates of bioturbation—decreased sedimentary retention of pyrite.

4.2.1. Sulfur-carbon ratios in the Paleozoic rock record

To test the hypothesis that early bioturbation could have increased early Paleozoic pyrite burial efficiency, we compiled sulfur-organic carbon (S/TOC) ratios from the Sedimentary Geochemistry and Paleoenvironments (SGP) Phase 1 repository (Farrell et al., 2021; https://sgp-search.io/) from the Ediacaran through the present day. The use of S/TOC ratios normalizes sulfur burial to changes in TOC burial. While we expect that TOC burial has been a primary driver of Phanerozoic pyrite burial, our

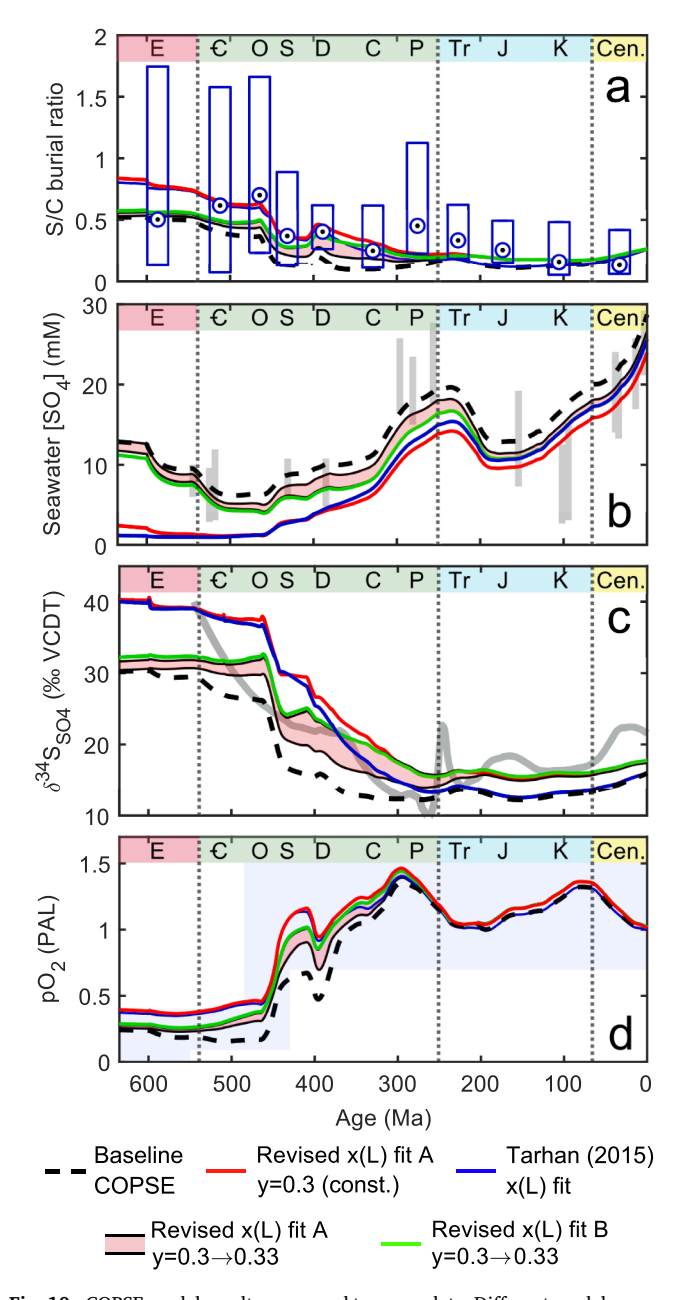


Fig. 10. COPSE model results compared to proxy data. Different model runs are described in Section 4.2 and in the Supplementary Material. Vertical dotted lines represent the beginnings of the Paleozoic, Mesozoic, and Cenozoic Eras. The colored band at the top of each panel indicates the Ediacaran (E), Cambrian (C), Ordovician (O), Silurian (S), Devonian (D), Carboniferous (C), Permian (P), Triassic (Tr), Jurassic (J), and Cretaceous (K) Periods, as well as the Cenozoic Era (Cen). (a) COPSE model results of pyrite sulfur/organic carbon (S/TOC) burial ratios and a histogram of S/TOC ratios in fine-grained marine siliciclastic rocks binned by geological age (Farrell et al., 2021). Histogram positions in the x-direction are aligned to the middle of each Period or Era. The upper and lower edge of each box marks the upper and lower quartile, respectively, and the circled point inside each box marks the median. (b) COPSE model outputs of seawater sulfate concentration compared to proxy data. The grey bars represent sulfate proxy data compiled in Lenton et al. (2018), with added data from Blättler et al. (2020). (c) COPSE model outputs of seawater sulfate δ^{34} S values compared to proxy data. The thick grey line represents a LOESS regression of the data set of Present et al. (2020) with bulk carbonate associated sulfate (CAS) data filtered out due to concerns about the validity of those data (Present et al., 2020). (d) COPSE model outputs of atmospheric pO2 (fraction of present atmospheric level) compared to proxy data. The shaded areas of the plot represent probable upper and lower bounds on atmospheric pO2 from Sperling et al. (2015) and Glasspool and Gastaldo (2022).

primary interest is in analyzing changes in pyrite burial relative to this baseline driver. When compiling SGP data for our analyses, we selected only fine-grained siliciclastic lithologies that were not assigned to terrestrial environments—i.e., marine claystones, shales, mudstones, and siltstones. We filtered the SGP data set for samples that had measurements for both TOC abundance (wt. %) and either S-py (wt. % pyrite sulfur) or S (wt. % sulfur) abundance; therefore, only samples that had both TOC and S/S-py data were included. Ratios of sulfur to TOC were binned according to the interpreted ages of samples listed in the SGP data base, with bin boundaries corresponding to the chronostratigraphic boundaries established by the International Commission on Stratigraphy (Cohen et al., 2013).

Compiled lithologic data should be interpreted with caution. One reason for this is that the SGP database is subject to certain biases in data sampling. The SGP Phase 1 repository contains individual contributions from submitting authors along with data from the U.S. Geological Survey Critical Metals in Black Shales project (USGS-CMIBS) and the U.S. Geological Survey National Geochemical Database (USGS-NGDB). As such, the full database primarily comprises North American samples (Farrell et al., 2021). Also, certain data sources may overrepresent individual geological formations that have been more extensively analyzed than others. For example, out of ~1370 sulfur concentration measurements of fine-grained marine siliciclastic rocks from the Ordovician Period, 517 (38 %) are sourced from USGS-CMIBS analyses of a single formation. This means that including or omitting CMIBS data has a strong effect on median Ordovician sulfur concentration, although the lack of paired TOC data from that formation means that the median Ordovician S/TOC ratio is much less affected (Fig. S9). In the Supplementary Information, we present more detail on the SGP data filtering procedure and potential biases.

Paired TOC and sulfur data from the SGP repository (n = 13818, or 6909 ratios) indicate that the median $(\mu_{1/2})$ S/TOC ratio of marine siliciclastic sediments increased from the Ediacaran ($\mu_{1/2} = 0.50, \, n = 688$) through the Cambrian ($\mu_{1/2} = 0.63$, n = 903) and the Ordovician ($\mu_{1/2} =$ 0.69, n = 548; Fig. 10a). After the Ordovician, median S/TOC ratios dropped sharply in the Silurian ($\mu_{1/2}=0.37,\,n=293$), Devonian ($\mu_{1/2}=0.37,\,n=293$), 0.40, n = 1813), and Carboniferous ($\mu_{1/2}=$ 0.25, n = 1292), increased again in the Permian ($\mu_{1/2} = 0.44$, n = 541), and then declined through the rest of the Phanerozoic. The 39 % increase in median S/TOC ratio from the Ediacaran to the Ordovician supports our hypothesis, but caution is warranted in interpreting these data for two reasons. First, the absolute change in median S/TOC from the Ediacaran through the Ordovician is small compared to the interquartile ranges of the pre-Silurian data bins; second, there may be biases in the SGP data set as discussed above. For example, omitting USGS-CMIBS data from the analysis generates an earlier S/TOC peak in the Cambrian followed by a more gradational decrease of S/TOC into the Ordovician and Silurian (Fig. S9). Nonetheless, two prominent features of this data set-an increase in median S/TOC ratios in the Cambrian relative to the Ediacaran and a permanent decrease in S/TOC variability by the Silurian-Devonian-appear to be broadly robust to different filtering criteria. These data also corroborate previous observations of high Cambro-Ordovician S/TOC ratios relative to later Phanerozoic sediments (Berner, 1984). We suggest that early bioturbation could have increased the rate of sulfur burial per unit of organic carbon burial. The amount of oxygen added by greater pyrite burial efficiency can be roughly estimated with a simple calculation based on the stoichiometry of oxygen release from the burial of organic carbon (1:1) versus pyrite (15:8) (Canfield, 2005). If we compare the median Ordovician S/TOC of 0.69 to a scenario in which Ordovician sediments retained the Ediacaran S/TOC ratio of 0.50, the S/TOC ratio of 0.69 should release 18 % more O2 per unit of TOC burial than the ratio of 0.50.

The permanent decrease in the variability of S/TOC ratios across the Ordovician-Silurian boundary suggests a secular change in the carbon and sulfur cycles that has persisted for the rest of the Phanerozoic. The Ordovician-Silurian shift to lower and more homogenous S/TOC ratios does not correspond to a rapid change in sediment mixed layer depth, which increased only from 1 cm to 1.5 cm in this interval (Tarhan et al., 2015). Instead, it is more probable that increases in Silurian pO_2 spurred by vascular land plants (Krause et al., 2018; Lenton et al., 2018; Tostevin and

Mills, 2020) led to more homogeneously oxidized water column conditions across shelf and slope environments. This redox homogenization would have led to less variability in sedimentary biogeochemical cycling, which in turn would have reduced global sedimentary S/TOC variability. However, as described above, higher S/TOC ratios themselves would have contributed to oxygen buildup through the Cambrian and Ordovician. The lower O2 concentrations of the Cambro-Ordovician would have permitted more efficient transfer of organic carbon to sediments (Hartnett et al., 1998), but the TOC-normalized sulfur data suggest more efficient pyritization per unit of TOC. We caution that there is not always a clear distinction between early Paleozoic formations with bioturbated sediments and those with nonburrowed sediments under euxinic water; for example, the Cambrian Alum Shale contains trilobite fossils interspersed with geochemical evidence for euxinia (Dahl et al., 2019). However, it is possible that these oscillating conditions, apparently a distinctive feature of the early Paleozoic (Pruss and Gill, 2024), could have spurred greater fluxes of pyrite precipitation, as suggested for our core 4.3W. In general, the SGP data suggest that the Cambrian and Ordovician Periods represent a distinct interval of the Proterozoic-Phanerozoic transition in which early bioturbation increased the efficiency of pyrite burial, but after which increasing pO₂ led to a homogenization of the global sedimentary carbon-sulfur cycle.

4.2.2. Modeling sulfide retention and seawater-sediment sulfate transfer

Data from the Chesapeake Bay suggest that mild oxidation could have increased the efficiency of early Paleozoic pyrite precipitation—yet on a global scale, oxygen accumulation eventually would have impeded pyrite burial. To explore this feedback in more detail, we modified the pyrite burial term in the COPSE biogeochemical model (Lenton et al., 2018) by adding parameters from the model of Canfield and Farquhar (2009). The two prongs of our hypothesis—increased sedimentary sulfide retention and increased sedimentary sulfate supply—are expressed in the latter model with the function

$$F_{b-pyr} = x \cdot a \cdot OC \cdot [SO_4]^y$$
(3)

where $F_{b\text{-}pyr}$ is the global pyrite burial flux, x is the fraction of reduced sedimentary sulfide that is retained in sediment as pyrite, a is a constant of proportionality, OC is the concentration of sedimentary organic carbon, [SO₄] is seawater sulfate concentration, and y is an exponent that modulates the sedimentary sulfate reservoir relative to the size of the seawater sulfate reservoir. Thus, the variable x denotes sedimentary sulfide retention in the form of pyrite and the variable y denotes the availability of seawater sulfate to sulfate reducing microorganisms in sediments. In effect, y converts the seawater sulfate reservoir to a depthintegrated reservoir of the pore water sulfate that can be reduced by sulfate reducing microorganisms. Its value reflects both the efficiency of sulfate transfer from the seawater reservoir to the pore water reservoir and the efficiency of pore water sulfate utilization by sulfate reducing microorganisms, which can be affected by differences in the sedimentary depth distributions of TOC and sulfate.

In previous modeling studies (Canfield and Farguhar, 2009; Tarhan et al., 2015), the value of y has been assumed to remain constant over time. However, as detailed in the Introduction, bioturbation tends to increase gross rates of sedimentary sulfate reduction and the rate of sulfate transfer from seawater to sediments—suggesting that the value of y should have increased in the Paleozoic. At the same time, bioturbation also changes the value of x by transferring oxidants into sediments. Under modern pO2 and modern bioturbation intensity, these oxidant fluxes are more likely to lower the value of x and suppress pyrite preservation. However, mild sediment mixing and increasing bottom-water oxygenation in the early Paleozoic would have increased the value of x by trapping reactive Fe- and Mn-oxides in shallow sediments (Aller, 1994; Middelburg and Levin, 2009; Beam et al., 2022). These compounds can partially oxidize sulfide and FeS to ZVS compounds (Schippers and Jørgensen, 2001; Poulton et al., 2004; Avetisyan et al., 2021), thus retaining sulfur in the sediment in a form that can precipitate pyrite via the polysulfide pathway. Generation of ZVS compounds might have been promoted by sulfide oxidizing microbes such

as Beggiatoa, which in some sediments can contribute to rapid pyrite precipitation (Hantsoo et al., 2023). Sediment incubations with polychaetes indicate that bioturbation increases the sulfate flux into sediments and also increases the sulfide flux out of sediments (Riemer et al., 2023), but the higher sulfide efflux does not necessarily mean that the value of x is decreasing. Higher sulfide fluxes out of bioturbated sediment may be directly proportional to the increased sulfate reduction rates permitted by bioturbation (i.e., no change in x and an increase in y). It is also plausible that lower sulfide retention may be compensated by a higher sulfate reduction rate (decreasing x and increasing y), or that greater sulfate availability may act in tandem with the creation of ZVS compounds that promote pyrite precipitation (increasing x and increasing y). Our hypothesis does not specifically address the possible effects of early bioturbation on pyrite formation associated with SMT or sub-SMT sediments. However, unless early bioturbation simultaneously induced a proportional decrease in SMT-associated pyrite precipitation at the same time as the hypothesized increase in shallower pyrite precipitation—which we consider unlike--then net pyrite burial would have increased.

To explore the effects of these changes, we added the terms x and y from Eq. (3) to the COPSE model as boundary conditions. Because x has changed over the Phanerozoic, we used the method of Tarhan et al. (2015) in which a curve fit of sulfide retention (x) versus mixed layer depth (L, cm) from modern sediments is substituted into a curve fit of mixed layer depth evolution over Phanerozoic time (t). In other words, this method substitutes an x(L) function into an L(t) function to yield an x(t) function (Fig. S10). We removed two x-L data points at L = 0 from the Tarhan et al. (2015) compilation because those sites appear to be subject to strong physical forcings such as extreme sedimentation rates and extensive reworking by wave action (Chanton et al., 1987; Ruttenberg, 1990). We added a new x-L data point from site 4.3W, with a range of x estimates from Roden and Tuttle (1993) and an L estimate from Hantsoo et al. (2023). Uncertainty in the value of x at site 4.3W is reflected in the shaded red areas in Fig. 10, and the tests that used x-L data from site 4.3W were termed 'Revised x(L) fit A' (Fig. S10b). A different polynomial curve, which we designate 'Revised x(L) fit B,' used the x-value of 0.25 from 4.3W as well as x-L estimates from two additional sites: 4.3C and 3.1. The estimates of x from site 4.3C (x = 0.29) and site 3.1 (x = 0.56) are drawn from Roden and Tuttle (1993) and Marvin-DiPasquale and Capone (1998), respectively. The value of x at site 3.1 is probably overestimated, as the nearby site studied in Marvin-DiPasquale and Capone (1998) had lower salinity and a higher sedimentation rate; nonetheless, we found that adding these two data points to the polynomial fit did not cause significant changes in the model results (Fig. 10; Fig. S14). Finally, we ran sensitivity tests of y(t), including the original static values of y (0.3, 0.5, and 0.75; Canfield and Farguhar, 2009) as well as initial y-values that increased or decreased to different values over time (Figs. S11-S13). The constant-y models generally do not perform as well in reproducing the [SO₄] and $\delta^{34}S_{SO4}$ records as the varying-y models. Additionally, decreasing y or increasing it more than 10 % also leads to poor model-proxy fits (Figs. S11-S12). However, setting y equal to 1 (thus omitting y) yields much more accurate results than the other constant-y models (Fig. S13). The constant y = 1 model has similar root mean square errors as the varying-y 'Revised x(L) fit A' model for sulfate concentration and sulfate $\delta^{34}S$ values, but the latter model has a slightly better root mean square errors for S/C burial (Fig. S13). For simplicity, all changes in y were assumed to be linear between 540 and 200 Ma; the latter date reflects the attainment of near-modern mixed layer depths (Buatois et al., 2016). Our derivation of the x(t) and y(t) curves and the exact modifications made to the COPSE code are described in more detail in the Supplementary Information.

Here we focus on the results of three model scenarios, the first one with a variable value of y and two others with static values of y. The first scenario ('Revised x(L) fit A,' the pink shaded area in Fig. 10) includes x(t) curves derived from the low and high x-values (0.18 and 0.32) at site 4.3W, along with a y-value that increases linearly from 0.3 at 540 Ma to 0.33 at 200 Ma. The second scenario (the red line in Fig. 10) includes the x(t) fit to the mid-range value of x (0.25) from site 4.3W and an unvarying value of y = 0.3. The third scenario (the blue line in Fig. 10) uses the original x(t)

model of Tarhan et al. (2015) and the static y-value of 0.75 used in that study. These results are plotted alongside the baseline COPSE model (Lenton et al., 2018; the dashed black lines in Fig. 10), in which x and y are both set to 1 by default. We report COPSE outputs for S/TOC ratios, seawater sulfate concentrations, seawater sulfate $\delta^{34}{\rm S}$ values, and $p{\rm O}_2$ over the Phanerozoic. The COPSE model adds 2 mol of ${\rm O}_2$ to the atmospheric reservoir for each mole of pyrite sulfur that is buried, and seawater SO4 $\delta^{34}{\rm S}$ values in the baseline COPSE model vary as a function of the relative rates of pyrite burial versus total sulfur burial, while the 'instantaneous' fractionation between seawater sulfate and buried pyrite is held constant at 35 ‰. Equation (3) changes the pyrite burial flux term in COPSE, but no other parts of the model have been changed.

How well do the models match proxy data for S/TOC ratios, seawater sulfate concentrations, seawater sulfate $\delta^{34} S$ values, and $pO_2?$ To answer this question, model-proxy matches were compared statistically by means of root mean squared error (RMSE) analyses. Compared to 'Revised x(L) fit A,' the baseline COPSE model generates a substantially better fit for [SO_4], but a substantially worse fit for S/C and $\delta^{34} S_{SO4}$ records (Fig. S14). 'Revised x(L) fit A' generates a better RMSE fit for [SO_4] and $\delta^{34} S_{SO4}$ records than the other primary revised models, but a worse fit for S/C ratios (Fig. S14). We regard 'Revised x(L) fit A' as the best match to the tested proxy data because it has lower RMSE values in at least two out of three proxies when compared to each other model run, although it does not surpass any other model run in all three proxies. More detailed comparisons for each proxy system are presented in the following paragraphs.

Results show that none of the COPSE model formulations increases the S/TOC burial rate in the Cambro-Ordovician relative to the Ediacaran, although the variable-y model performs best at damping the relative decrease (Fig. 10a). The drop in modeled S/TOC ratios primarily results from a large (\sim 25 %) increase in organic carbon burial that occurs in the Cambrian in the baseline version of COPSE and is conserved in all of the modified versions. The models with static values of y do the best at replicating S/TOC ratios for the Cambrian through the Carboniferous, but this subset of models also features high Ediacaran S/TOC ratios that decrease into the early Paleozoic, in contrast to the SGP data set. The models with unchanging values of y (aside from the baseline COPSE model) produce oceanic sulfate concentrations that are well below proxy values throughout the Paleozoic, including concentrations below 2 mM in the Cambro-Ordovician (Fig. 10b). Thus, the baseline COPSE model and the varyingy model perform much better in matching the proxy [SO₄] record in the latest Ediacaran and the early Paleozoic; this is a notable advantage over the static-y models.

Meanwhile, the seawater sulfate δ^{34} S curve is more ambiguous and features tradeoffs in the accuracy of each model depending on which time interval is being considered (Fig. 10c). None of the models provides strong agreement with the δ^{34} S proxy record throughout the Ediacaran and Paleozoic. High Ediacaran seawater sulfate δ^{34} S values are an unusual feature, but mass balance predicts that they should have resulted from higher pyrite burial fluxes and/or from greater isotopic fractionation between sulfate and sulfide (Fike et al., 2015). Biodiffusion in the late Ediacaran was low but non-zero-possibly 10 % of early Cambrian values (Cribb et al., 2023)—and it is unclear whether such low biodiffusion rates could have increased pyrite burial fluxes by the mechanism described in this study. Global changes in sulfate-sulfide isotopic fractionation are difficult to assess in deep time (Krause et al., 2018), but high Ediacaran-Cambrian seawater sulfate δ^{34} S values may have resulted from increasing microbial oxidative sulfur cycling in sediments (Kunzmann et al., 2017). This change in fractionation would not be captured by the baseline COPSE model, which assumes a constant seawater-pyrite fractionation.

The variable-y model ('Revised x(L) fit A') creates the most realistic pO_2 curve for the early Paleozoic (Fig. 10d). Evidence for fires in the rock record point to a pO_2 of at least 70 % of present atmospheric level (PAL) by the Early Devonian (Belcher and McElwain, 2008; Sperling et al., 2015), and recent evidence of charcoal from Middle Silurian rocks may push the 70 % PAL threshold back to ~430 Ma (Glasspool and Gastaldo, 2022). A paucity of charcoal in Late Devonian rocks raises the possibility that pO_2 dipped back below 70 % PAL in that interval (Scott and Glasspool, 2006), but it is

unclear whether this gap results from low oxygen or from preservational biases (Mills et al., 2023). Thus, to conform to the charcoal record, an Earth system biogeochemical model should exceed 70 % PAL by the Middle Silurian; a temporary decline below 70 % in the Late Devonian may also be acceptable, though this is less certain. Results show that the baseline COPSE model does not exceed 70 % PAL until the Late Devonian, while the L-x fit from Tarhan et al. (2015) and the revised L-x fit with an unchanging y value both maintain pO_2 well above 90 % PAL throughout the Late Devonian. The variable-y model generates an intermediate pO_2 curve that best fits the charcoal record, exceeding 70 % PAL by the Middle Silurian and reaching a local minimum of 70–85 % PAL in the Middle Devonian.

To summarize the model-proxy comparisons, the baseline COPSE model and the variable-y models perform much better than the static-y models in replicating the Paleozoic [SO₄] proxy record. The variable-y models improve upon baseline COPSE in replicating the pO2 proxy record of the Silurian and Devonian. None of the models increases S/TOC from the Ediacaran through the early Paleozoic, but the Tarhan et al. (2015) x(L) fit best replicates SGP-derived S/TOC burial ratios for the Cambrian, Silurian, Devonian, and Carboniferous. All of the revised models offer modest improvements over the baseline COPSE model in replicating the Paleozoic seawater sulfate $\delta^{34}S$ proxy record, but they all deviate substantially from the seawater sulfate $\delta^{34}S$ record in certain intervals. From the low RMSE values generated by 'Revised x(L) fit A,' we conclude that a gradual increase (10 % from 540-200 Ma) in the value of the parameter y and a transient Paleozoic increase in the value of x generate a better fit to early Paleozoic pO₂ constraints than the baseline COPSE model. This combination also provides better RMSE fits than each other model run in at least two out of three tested proxy systems. However, there are still important discrepancies between this model and certain proxy data-—particularly the seawater sulfate δ^{34} S record and the S/TOC record—that will require further work to resolve.

5. Conclusions

To better understand controls on pyrite accumulation in dynamic, lowoxygen environments, we collected nine sediment cores from the Chesapeake Bay, a large estuary with strong gradients in salinity, hypoxia intensity, organic matter provenance and abundance, and bioturbation. We found that pyrite precipitation from its potential precursor FeS was impeded in the northern Chesapeake Bay, an effect that we attribute to a lack of sulfur redox intermediates under reducing, sulfate-limited conditions. The isotopic profiles of pyrite and its precursor compounds along SO₄/Cl gradients suggested a prominent role for the polysulfide reaction pathway in shallow Chesapeake Bay sediments, but the H2S reaction pathway appears more prominent in association with sulfate-methane transition zones at three of the northern sites. We also found that pyrite was most abundant in sediment cores that lay in the mid-range of pore water SO₄/Cl ratios. These findings lead us to propose that pyrite accumulation is limited when microbial sulfate demand in reducing, TOC-rich sediments—particularly fine-grained and non-burrowed iments—cannot be matched by sulfate replenishment from the water column. In comparison, mild to moderate bioturbation may increase pyrite burial by increasing the net flux of sulfate into the sediments, and/or by increasing the sulfide retention of the sediment column. The former is a well-documented effect; the latter may be accomplished by partially oxidizing and trapping sulfide as ZVS in shallow sediments, at which point it can precipitate pyrite via the polysulfide pathway.

Applying this line of reasoning to the early Paleozoic Era, we hypothesize that pyrite burial per unit of TOC burial increased during the protracted onset of bioturbation. This increase in pyrite burial efficiency would have been temporary because intensifying bioturbation, in concert with rising pO_2 , eventually would have introduced enough oxidizing power into the sediment pile to suppress pyrite retention. In support of our hypothesis, a database compilation of paired sulfur-carbon ratios of finegrained marine siliciclastic rocks indicates an increase in median S/TOC ratios from the Ediacaran through the Ordovician. After this increase, median S/TOC ratios decreased in the Silurian and have remained much

less variable for the rest of the Phanerozoic Eon. The much lower variability of post-Ordovician S/TOC ratios suggests that $p\mathrm{O}_2$ rose to a sufficient level to homogenize the linked sedimentary carbon and sulfur cycles by the Silurian

Finally, we modified the pyrite burial term in the COPSE biogeochemical model (Lenton et al., 2018) by adding two parameters from the box model of Canfield and Farquhar (2009). The first parameter (x) expresses sedimentary sulfide retention, while the second parameter (y) expresses the availability of seawater sulfate to microbial sulfate reduction in sediments. We introduced a revised fit of sulfide retention rates versus sediment mixed layer depths with a new data point from the Chesapeake Bay. We also allowed the value of y to increase gradually over Phanerozoic time as a function of increasing sediment mixed layer depth; this parameter previously had been modeled as a static value. The revised COPSE model that included a transient Paleozoic increase in x and a gradual but permanent 10 % increase in y generated an oxygen curve that matched pO_2 proxy constraints more closely than the baseline COPSE model, particularly in the Silurian and Devonian Periods.

We conclude that greater sulfate supply to sediments and greater prevalence of sulfur redox intermediates can promote pyrite burial in modern sediments. This implies that bioturbation in the early Paleozoic Era could have increased the flux of pyrite burial per unit of organic carbon burial. Although this hypothesis contrasts with previous models of Paleozoic sulfur cycling, it appears consistent with compiled geochemical data and biogeochemical model results. While further work is needed to refine our knowledge of how mild bioturbation can affect pyrite burial and other aspects of biogeochemical cycling, our results imply that an increase in pyrite burial efficiency could have acted as a temporary positive feedback on early Paleozoic ocean–atmosphere oxygenation until pO_2 reached sufficient levels to stabilize S/TOC burial ratios in the Silurian Period.

Data availability

Supplementary Files are available from the Johns Hopkins University Research Data Repository at https://doi.org/10.7281/T1/VNFY91.

CRediT authorship contribution statement

Kalev Hantsoo: Writing – review & editing, Writing – original draft, Funding acquisition, Data curation, Conceptualization. Maya Gomes: Writing – review & editing, Writing – original draft, Resources, Funding acquisition, Data curation, Conceptualization. Dana Brenner: Writing – review & editing, Methodology, Data curation. Jeffrey Cornwell: Writing – review & editing, Resources, Methodology. Cindy M. Palinkas: Writing – review & editing, Resources, Methodology. Sairah Malkin: Writing – review & editing, Resources, Methodology.

Declaration of competing interest

The authors declare that they have no known competing financial interests or personal relationships that could have appeared to influence the work reported in this paper.

Acknowledgments

This work was funded by a grant from the American Chemical Society Petroleum Research Fund (ACS PRF# 60407-DNI2) to MG, a Johns Hopkins University Department of Earth and Planetary Sciences Field Work Grant to KH, and a Johns Hopkins University Provost's Office COVID Relief Dissertation Completion fellowship to KH. The authors wish to thank Minming Cui, Pinky Liau, Carol Kim, Greg Silsbe, Kabir Mohammed, Jacob Cram, Clara Fuchsman, and the crew of the *R/V Rachel Carson* for assistance with core collection and processing; Andy Masterson for helpful discussion of analytical methods; and Michael Yoo, Emily Portillo, and Ali Luchs for assistance with sample preparation. The authors also wish to thank Ted Present, Jiarui Liu, and an anonymous reviewer for comments that greatly improved the manuscript.

Appendix A. Supplementary material

The Supplementary Material is a document that includes additional figures as well as text that describes the collected sediment cores, the SGP data set, and the COPSE model modifications in greater detail. In addition to this document, Supplementary Files are available in an open source data repository (see "Data Availability"). The files in the data repository include (a) the geochemical data collected from the Chesapeake Bay sediment cores, (b) Matlab code and associated Matlab vector arrays that can be added to the baseline COPSE model, and (c) a filtered version of the SGP data download and a description of the filtering process used on that data set. Supplementary material to this article can be found online at htt ps://doi.org/10.1016/j.gca.2024.04.018.

References

- Aller, R.C., 1994. The sedimentary Mn cycle in Long Island Sound: Its role as intermediate oxidant and the influence of bioturbation, O_2 , and C_{org} flux on diagenetic reaction balances. J. Marine Res. 52 (2), 259–295.
- Aller, R.C., Yingst, J.Y., 1978. Biogeochemistry of tube-dwellings: a study of the sedentary polychaete Amphitrite ornata (Leidy). J. Mar. Res. 36, 201–254.
- Amrani, A., Kamyshny, A., Lev, O., Aizenshtat, Z., 2006. Sulfur stable isotope distribution of polysulfide anions in an (NH4)2Sn aqueous solution. Inorg. Chem. 45 (4), 1427–1429.
- Antler, G., Mills, J.V., Hutchings, A.M., Redeker, K.R., Turchyn, A.V., 2019. The sedimentary carbon-sulfur-iron interplay—A lesson from East Anglian salt marsh sediments. Front. Earth Sci. 7, 140.
- Appleby, P.G., Oldfield, F., 1978. The calculation of lead-210 dates assuming a constant rate of supply of unsupported 210 Pb to the sediment. Catena 5 (1), 1–8.
- Arndt, S., Jørgensen, B.B., LaRowe, D.E., Middelburg, J.J., Pancost, R.D., Regnier, P., 2013.

 Quantifying the degradation of organic matter in marine sediments: A review and synthesis. Earth-Sci. Rev. 123. 53–86.
- Avetisyan, K., Buchshtav, T., Kamyshny Jr, A., 2019. Kinetics and mechanism of polysulfides formation by a reaction between hydrogen sulfide and orthorhombic cyclooctasulfur. Geochim. Cosmochim. Acta 247, 96–105.
- Avetisyan, K., Zweig, I., Luther, G.W., Kamyshny Jr, A., 2021. Kinetics and mechanism of polysulfides and elemental sulfur formation by a reaction between hydrogen sulfide and δ -MnO₂. Geochim. Cosmochim. Acta 313, 21–37.
- Beam, J.P., Michaud, A.B., Johnston, D.T., Girguis, P.R., Emerson, D., 2022. Impacts of bioturbation on iron biogeochemistry and microbial communities in coastal sediment mesocosms under varying degrees of hypoxia. Estuar. Coast Shelf Sci. 276, 108032.
- Belcher, C.M., McElwain, J.C., 2008. Limits for combustion in low $\rm O_2$ redefine paleoatmospheric predictions for the Mesozoic. Science 321 (5893), 1197–1200.
- Berner, R.A., 1970. Sedimentary pyrite formation. Am. J. Sci. 268 (1), 1–23.
- Berner, R.A., 1980. Early diagenesis: a theoretical approach. Princeton University Press, Princeton, NJ.
- Berner, R.A., 1982. Burial of organic carbon and pyrite sulfur in the modern ocean: its geochemical and environmental significance. Am. J. Sci. 282, 451–473.
- Berner, R.A., 1984. Sedimentary pyrite formation: an update. Geochim. Cosmochim. Acta 48 (4), 605–615.
- Berner, R.A., Baldwin, T., Holdren, G.R., 1979. Authigenic iron sulfides as paleosalinity indicators. J. Sediment. Res. 49 (4), 1345–1350.
- Berner, R.A., Raiswell, R., 1983. Burial of organic carbon and pyrite sulfur in sediments over Phanerozoic time: a new theory. Geochim. Cosmochim. Acta 47 (5), 855–862.
- Berner, R.A. (1974). Iron sulfides in Pleistocene deep Black Sea sediments and their paleo-oceanographic significance. In: Degens, E.T., Ross, D.A. (Eds.), The Black Sea: Geology, Chemistry and Biology. Memoir of the American Association of Petroleum Geologists, vol. 20, pp. 524 531.
- Bertics, V.J., Ziebis, W., 2010. Bioturbation and the role of microniches for sulfate reduction in coastal marine sediments. Environ. Microbiol. 12 (11), 3022–3034.
- Bertics, V.J., Sohm, J.A., Treude, T., Chow, C.E.T., Capone, D.G., Fuhrman, J.A., Ziebis, W., 2010. Burrowing deeper into benthic nitrogen cycling: the impact of bioturbation on nitrogen fixation coupled to sulfate reduction. Mar. Ecol. Prog. Ser. 409, 1–15.
- Blättler, C.L., Bergmann, K.D., Kah, L.C., Gómez-Pérez, I., Higgins, J.A., 2020. Constraints on Meso-to Neoproterozoic seawater from ancient evaporite deposits. Earth Planet. Sci. Lett. 532, 115951.
- Bonaglia, S., Marzocchi, U., Ekeroth, N., Brüchert, V., Blomqvist, S., Hall, P.O., 2019. Sulfide oxidation in deep Baltic Sea sediments upon oxygenation and colonization by macrofauna. Mar. Biol. 166, 1–12.
- Böning, P., Brumsack, H.J., Böttcher, M.E., Schnetger, B., Kriete, C., Kallmeyer, J., Borchers, S.L., 2004. Geochemistry of Peruvian near-surface sediments. Geochim. Cosmochim. Acta 68 (21), 4429–4451.
- Borowski, W.S., Paull, C.K., Ussler III, W., 1999. Global and local variations of interstitial sulfate gradients in deep-water, continental margin sediments: Sensitivity to underlying methane and gas hydrates. Mar. Geol. 159 (1–4), 131–154.
- Bottjer, D.J., Hagadorn, J.W., Dornbos, S.Q., 2000. The Cambrian substrate revolution. GSA Today 10 (9), 1–7.
- Boudreau, B.P., 1998. Mean mixed depth of sediments: the wherefore and the why. Limnol. Oceanogr. 43 (3), 524–526.
- Boudreau, B.P., Westrich, J.T., 1984. The dependence of bacterial sulfate reduction on sulfate concentration in marine sediments. Geochim. Cosmochim. Acta 48 (12), 2503–2516.

- Boyle, R.A., Dahl, T.W., Dale, A.W., Shields-Zhou, G.A., Zhu, M.Y., Brasier, M.D., Canfield, D.E., Lenton, T.M., 2014. Stabilization of the coupled oxygen and phosphorus cycles by the evolution of bioturbation. Nat. Geosci. 7 (9), 671–676.
- Brush, G.S., 2001. Natural and anthropogenic changes in Chesapeake Bay during the last 1000 years. Hum. Ecol. Risk Assess. 7 (5), 1283–1296.
- Bryant, R.N., Houghton, J.L., Jones, C., Pasquier, V., Halevy, I., Fike, D.A., 2023. Deconvolving microbial and environmental controls on marine sedimentary pyrite sulfur isotope ratios. Science 382 (6673), 912–915.
- Buatois, L. A., Carmona, N. B., Curran, H. A., Netto, R. G., Mángano, N. G., and Wetzel, A. (2016). The Mesozoic Marine Revolution. In: Mangano, M.G., Buatois, L.A. (Eds.), The Trace Fossil Record of Major Evolutionary Events, vol. 2. Dordrecht: Topics in Geobiology, 40, 18–134.
- Buatois, L.A., Mángano, M.G., Minter, N.J., Zhou, K., Wisshak, M., Wilson, M.A., Olea, R.A., 2020. Quantifying ecospace utilization and ecosystem engineering during the early Phanerozoic—The role of bioturbation and bioerosion. Sci. Adv. 6 (33), eabb0618.
- Butler, I.B., Böttcher, M.E., Rickard, D., Oldroyd, A., 2004. Sulfur isotope partitioning during experimental formation of pyrite via the polysulfide and hydrogen sulfide pathways: implications for the interpretation of sedimentary and hydrothermal pyrite isotope records. Earth Planet. Sci. Lett. 228 (3-4), 495-509.
- Byrne, R.J., Hobbs, C.H., Carron, M.J. (1982). Baseline Sediment Studies to Determine Distribution, Physical Properties, Sedimentation Budgets and Rates in the Virginia Portion of the Chesapeake Bay. Virginia Institute of Marine Science, College of William and Mary, Gloucester Point, Virginia.
- Canfield, D.E., 2005. The early history of atmospheric oxygen: homage to Robert M. Garrels.
 Annu. Rev. Earth Planet. Sci. 33, 1–36.
- Canfield, D.E., Farquhar, J., 2009. Animal evolution, bioturbation, and the sulfate concentration of the oceans. Proc. Natl. Acad. Sci. 106 (20), 8123–8127.
- Canfield, D.E., Thamdrup, B., Fleischer, S., 1998. Isotope fractionation and sulfur metabolism by pure and enrichment cultures of elemental sulfur-disproportionating bacteria. Limnol. Oceanogr. 43 (2), 253–264.
- Canfield, D.E., Kristensen, E., Thamdrup, B., 2005. The sulfur cycle. In: Canfield, D.E., Kristensen, E., Thamdrup, B. (Eds.), Aquatic Geomicrobiology. Elsevier Academic Press, San Diego.
- Carbone, C., Narbonne, G.M., 2014. When life got smart: the evolution of behavioral complexity through the Ediacaran and early Cambrian of NW Canada. J. Paleontol. 88 (2), 309–330.
- Chanton, J.P., Martens, C.S., Goldhaber, M.B., 1987. Biogeochemical cycling in an organic-rich coastal marine basin. 7. Sulfur mass balance, oxygen uptake and sulfide retention. Geochim. Cosmochim. Acta 51 (5) 1187–1199.
- Claypool, G.E., 2004. Ventilation of marine sediments indicated by depth profiles of pore water sulfate and δ³⁴S. In: Geochemical Society Special Publications, Vol. 9. Elsevier, pp. 59–65.
- Cohen, K.M., Finney, S.C., Gibbard, P.L., Fan, J.-X., 2013. The ICS International Chronostratigraphic Chart. Episodes 36, 199–204.
- Cole, D.B., Mills, D.B., Erwin, D.H., Sperling, E.A., Porter, S.M., Reinhard, C.T., Planavsky, N.J., 2020. On the co-evolution of surface oxygen levels and animals. Geobiology 18 (3), 260–281.
- Colman, S.M., Halka, J.P., Hobbs III, C.H., Mixon, R.B., Foster, D.S., 1990. Ancient channels of the Susquehanna River beneath Chesapeake Bay and the Delmarva peninsula. Geol. Soc. Am. Bull. 102 (9), 1268–1279.
- Colman, S.M., Baucom, P.C., Bratton, J.F., Cronin, T.M., McGeehin, J.P., Willard, D., Zimmerman, A.R., Vogt, P.R., 2002. Radiocarbon dating, chronologic framework, and changes in accumulation rates of Holocene estuarine sediments from Chesapeake Bay. Ouat. Res. 57 (1), 58–70.
- Cooper, S.R., Brush, G.S., 1991. Long-term history of Chesapeake Bay anoxia. Science 254 (5034), 992–996.
- Cornwell, J.C., Sampou, P.A., 1995. Environmental controls on iron sulfide mineral formation in a coastal plain estuary. In: Vairavamurthy, M.A., Schoonen, M.A.A. (Eds.), Geochemical transformations of sedimentary sulfur. American Chemical Society, Washington, DC, pp. 224–242.
- Cornwell, J.C., Conley, D.J., Owens, M., Stevenson, J.C., 1996. A sediment chronology of the eutrophication of Chesapeake Bay. Estuaries 19 (2), 488–499.
- Cribb, A.T., van de Velde, S.J., Berelson, W.M., Bottjer, D.J., Corsetti, F.A., 2023. Ediacaran-Cambrian bioturbation did not extensively oxygenate sediments in shallow marine ecosystems. Geobiology 21, 435–453.
- Cronin, T.M., Dwyer, G.S., Kamiya, T., Schwede, S., Willard, D.A., 2003. Medieval warm period, little ice age and 20th century temperature variability from Chesapeake Bay. Glob. Planet. Change 36 (1–2), 17–29.
- Cutshall, N.H., Larsen, I.L., Olsen, C.R., 1983. Direct analysis of ²¹⁰Pb in sediment samples: self-absorption corrections. Nucl. Instrum. Methods Phys. Res. 206 (1–2), 309–312.
- Dahl, T.W., Siggaard-Andersen, M.L., Schovsbo, N.H., Persson, D.O., Husted, S., Hougård, I. W., Dickson, A.J., Kjær, K., Nielsen, A.T., 2019. Brief oxygenation events in locally anoxic oceans during the Cambrian solves the animal breathing paradox. Sci. Rep. 9 (1), 11669.
- Deng, L., Bölsterli, D., Kristensen, E., Meile, C., Su, C.C., Bernasconi, S.M., Seidenkrantz, M.-S., Glombitza, C., Lagostina, L., Han, X., Jørgensen, B.B., Røy, H., Lever, M.A., 2020. Macrofaunal control of microbial community structure in continental margin sediments. Proc. Natl. Acad. Sci. 117 (27), 15911–15922.
- Donald, R., Southam, G., 1999. Low temperature anaerobic bacterial diagenesis of ferrous monosulfide to pyrite. Geochim. Cosmochim. Acta 63 (13–14), 2019–2023.
- Drobner, E., Huber, H., Wächtershäuser, G., Rose, D., Stetter, K.O., 1990. Pyrite formation linked with hydrogen evolution under anaerobic conditions. Nature 346 (6286), 742–744
- Dunne, J.A., Williams, R.J., Martinez, N.D., Wood, R.A., Erwin, D.H., 2008. Compilation and network analyses of Cambrian food webs. PLoS Biology 6 (4), e102.
- Duverger, A., Berg, J.S., Busigny, V., Guyot, F., Bernard, S., Miot, J., 2020. Mechanisms of pyrite formation promoted by sulfate-reducing bacteria in pure culture. Front. Earth Sci. 8, 588310.

- Edwards, C.T., Fike, D.A., Saltzman, M.R., Lu, W., Lu, Z., 2018. Evidence for local and global redox conditions at an Early Ordovician (Tremadocian) mass extinction. Earth Planet. Sci. Lett. 481, 125–135.
- Farrell, Ú.C., Samawi, R., Anjanappa, S., Klykov, R., Adeboye, O.O., Agic, H., Ahm, A.-S.-C., Boag, T.H., Bowyer, F., Brocks, J.J., Brunoir, T.N., Canfield, D.E., Chen, X., Cheng, M., Clarkson, M.O., Cole, D.B., Cordie, D.R., Crockford, P.W., Cui, H., Sperling, E.A., 2021. The Sedimentary Geochemistry and Paleoenvironments Project. Geobiology 19, 545–556.
- Figueroa, M.C., van de Velde, S.J., Gregory, D.D., Lemieux, S., Drake, J., Treude, T., Kemnitz, N., Berelson, W., Choumiline, K., Bates, S., Kukkadapu, R., Fogel, M., Riedinger, N., Lyons, T.W., 2023. Early diagenetic processes in an iron-dominated marine depositional system. Geochim. Cosmochim. Acta 341, 183–199.
- Fike, D.A., Bradley, A.S., Rose, C.V., 2015. Rethinking the ancient sulfur cycle. Annu. Rev. Earth Planet. Sci. 43, 593–622.
- Findlay, A.J., Bennett, A.J., Hanson, T.E., Luther III, G.W., 2015. Light-dependent sulfide oxidation in the anoxic zone of the Chesapeake Bay can be explained by small populations of phototrophic bacteria. Appl. Environ. Microbiol. 81 (21), 7560–7569.
- Firsching, F.H., 1961. Precipitation of silver phosphate from homogenous solution. Anal. Chem. 33 (7), 873–874.
- Fossing, H., Jørgensen, B.B., 1990. Isotope exchange reactions with radiolabeled sulfur compounds in anoxic seawater. Biogeochemistry 9, 223–245.
- Gagnon, C., Mucci, A., Pelletier, É., 1995. Anomalous accumulation of acid-volatile sulphides (AVS) in a coastal marine sediment, Saguenay Fjord. Canada. Geochim. Cosmochim. Acta 59 (13), 2663–2675.
- Garrels, R.M., Perry, E.A., 1974. Cycling of carbon, sulfur, and oxygen through geologic time. The Sea 5, 303–336.
- Glasspool, I.J., Gastaldo, R.A., 2022. Silurian wildfire proxies and atmospheric oxygen. Geology 50 (9), 1048–1052.
- Goldhaber, M.B., Aller, R.C., Cochran, J.K., Rosenfeld, J.K., Martens, C.S., Berner, R.A., 1977. Sulfate reduction, diffusion, and bioturbation in Long Island Sound sediments; report of the FOAM Group. Am. J. Sci. 277 (3), 193–237.
- Gomes, M.L., Klatt, J.M., Dick, G.J., Grim, S.L., Rico, K.I., Medina, M., Ziebis, W., Kinsman-Costello, L., Sheldon, N.D., Fike, D.A., 2022. Sedimentary pyrite sulfur isotope compositions preserve signatures of the surface microbial mat environment in sediments underlying low-oxygen cyanobacterial mats. Geobiology 20 (1), 60–78.
- Guilbaud, R., Slater, B.J., Poulton, S.W., Harvey, T.H., Brocks, J.J., Nettersheim, B.J., Butterfield, N.J., 2018. Oxygen minimum zones in the early Cambrian ocean. Geochem. Perspect. Lett. 6, 33–38.
- Hagy, J.D., Boynton, W.R., Keefe, C.W., Wood, K.V., 2004. Hypoxia in Chesapeake Bay, 1950–2001: long-term change in relation to nutrient loading and river flow. Estuaries 27, 634–658.
- Halevy, I., Fike, D.A., Pasquier, V., Bryant, R.N., Wenk, C.B., Turchyn, A.V., Johnston, D.T., Claypool, G.E., 2023. Sedimentary parameters control the sulfur isotope composition of marine pyrite. Science 382 (6673), 946–951.
- Hantsoo, K., Gomes, M., Malkin, S., Brenner, D., Kenney, W.F., 2023. Sedimentary pyrite formation in a seasonally oxygen-stressed estuary: potential imprints of microbial ecology and position-specific isotope fractionation. J. Geophys. Res. Biogeosci., e2022JG007324
- Harding Jr, L.W., Meeson, B.W., Fisher Jr, T.R., 1986. Phytoplankton production in two east coast estuaries: photosynthesis-light functions and patterns of carbon assimilation in Chesapeake and Delaware Bays. Estuar. Coast. Shelf Sci. 23 (6), 773–806.
- Hartnett, H.E., Keil, R.G., Hedges, J.I., Devol, A.H., 1998. Influence of oxygen exposure time on organic carbon preservation in continental margin sediments. Nature 391 (6667), 572–575.
- Hedges, J.I., Keil, R.G., 1995. Sedimentary organic matter preservation: an assessment and speculative synthesis. Mar. Chem. 49 (2–3), 81–115.
- Hines, M.E., Jones, G.E., 1985. Microbial biogeochemistry and bioturbation in the sediments of Great Bay, New Hampshire. Estuar. Coast. Shelf Sci. 20 (6), 729–742.
- Holland, H.D., 1973. Systematics of the isotopic composition of sulfur in the oceans during the Phanerozoic and its implications for atmospheric oxygen. Geochim. Cosmochim. Acta 37 (12), 2605–2616.
- Holland, H.D., 1962. Model for the evolution of the Earth's atmosphere. In Petrologic Studies: A Volume in Honor of A.F. Buddington, ed. A. E. J. Engel, H. L. James, B. F. Leonard, pp. 447–77. Boulder, CO: Geol. Soc. Am.
- Holmkvist, L., Ferdelman, T.G., Jørgensen, B.B., 2011. A cryptic sulfur cycle driven by iron in the methane zone of marine sediment (Aarhus Bay, Denmark). Geochim. Cosmochim. Acta 75 (12), 3581–3599.
- Hurtgen, M.T., Lyons, T.W., Ingall, E.D., Cruse, A.M., 1999. Anomalous enrichments of iron monosulfide in euxinic marine sediments and the role of H₂S in iron sulfide transformations; examples from Effingham Inlet, Orca Basin, and the Black Sea. Am. J. Sci. 299 (7–9), 556–588.
- Jeong, H.Y., Han, Y.S., Park, S.W., Hayes, K.F., 2010. Aerobic oxidation of mackinawite (FeS) and its environmental implication for arsenic mobilization. Geochim. Cosmochim. Acta 74 (11), 3182–3198.
- Jin, C., Liao, Z., Lash, G.G., 2021. High-frequency redox variation across the Ordovician-Silurian transition, South China. Palaeogeogr. Palaeoclimatol. Palaeoecol. 566, 110218.
- Jørgensen, B.B., 1977. The sulfur cycle of a coastal marine sediment (Limfjorden, Denmark) 1. Limnol. Oceanogr. 22 (5), 814–832.
- Jørgensen, B.B., 1979. Å theoretical model of the stable sulfur isotope distribution in marine sediments. Geochim. Cosmochim. Acta 43 (3), 363–374.
- Jørgensen, B.B., 1982. Mineralization of organic matter in the sea bed—the role of sulphate reduction. Nature 296 (5858), 643–645.
- Jørgensen, B.B., 2021. Sulfur biogeochemical cycle of marine sediments. Geochem. Perspect. 10 (2), 145–307.
- Jørgensen, B.B., Parkes, R.J., 2010. Role of sulfate reduction and methane production by organic carbon degradation in eutrophic fjord sediments (Limfjorden, Denmark). Limnol. Oceanogr. 55 (3), 1338–1352.

- Jørgensen, B.B., Böttcher, M.E., Lüschen, H., Neretin, L.N., Volkov, I.I., 2004. Anaerobic methane oxidation and a deep H₂S sink generate isotopically heavy sulfides in Black Sea sediments. Geochim. Cosmochim. Acta 68 (9), 2095–2118.
- Jørgensen, B.B., Egger, M., Canfield, D.E., 2024. Sulfate distribution and sulfate reduction in global marine sediments. Geochim. Cosmochim. Acta 364, 79–88.
- Kamyshny Jr, A., Ferdelman, T.G., 2010. Dynamics of zero-valent sulfur species including polysulfides at seep sites on intertidal sand flats (Wadden Sea, North Sea). Mar. Chem. 121 (1–4), 17–26.
- Kamyshny, A., Goifman, A., Rizkov, D., Lev, O., 2003. Kinetics of disproportionation of inorganic polysulfides in undersaturated aqueous solutions at environmentally relevant conditions. Aquat. Geochem. 9, 291–304.
- Kamyshny, A., Goifman, A., Gun, J., Rizkov, D., Lev, O., 2004. Equilibrium distribution of polysulfide ions in aqueous solutions at 25 C: a new approach for the study of polysulfides' equilibria. Environ. Sci. Technol. 38 (24), 6633–6644.
- Kaplan, I.R., Emery, K.O., Rittenberg, S.G., 1963. The distribution and isotopic abundance of sulphur in recent marine sediments off southern California. Geochim. Cosmochim. Acta 27 (4), 297–331.
- Kemp, W.M., Boynton, W.R., Adolf, J.E., Boesch, D.F., Boicourt, W.C., Brush, G., Cornwell, J.C., Fisher, T.R., Glibert, P.M., Hagy, J.D., Harding, L.W., Houde, E.D., Kimmel, D.G., Miller, W.D., Newell, R.I.E., Roman, M.R., Smith, E.M., Stevenson, J.C., 2005. Eutrophication of Chesapeake Bay: historical trends and ecological interactions. Mar. Ecol. Prog. Ser. 303, 1–29.
- Kerhin, R., Halka, J.P., Wells, D.V., Hennessee, E.L., Blakeslee, P.J., Zoltan, N., Cuthbertson, R.H., 1988. The surficial sediments of Chesapeake Bay, Maryland: Physical characteristics and sediment budget. Investigative Report Number 48. Maryland Geological Survey, Baltimore, Maryland.
- Kerhin, R.T., Williams, C., Cronin, T.M., 1998. Lithologic descriptions of piston cores from Chesapeake Bay. US Geological Survey Open-file Report, Maryland, pp. 98–787.
- Kleinjan, W.E., De Keizer, A., Janssen, A.J., 2005a. Kinetics of the chemical oxidation of polysulfide anions in aqueous solution. Water Res. 39 (17), 4093–4100.
- Kleinjan, W.E., de Keizer, A., Janssen, A.J., 2005b. Equilibrium of the reaction between dissolved sodium sulfide and biologically produced sulfur. Colloids Surf. B 43 (3–4), 228–237.
- Knoll, A.H., Carroll, S.B., 1999. Early animal evolution: emerging views from comparative biology and geology. Science 284 (5423), 2129–2137.
- Kraal, P., Burton, E.D., Bush, R.T., 2013. Iron monosulfide accumulation and pyrite formation in eutrophic estuarine sediments. Geochim. Cosmochim. Acta 122, 75–88.
- Krause, A.J., Mills, B.J., Zhang, S., Planavsky, N.J., Lenton, T.M., Poulton, S.W., 2018.
 Stepwise oxygenation of the Paleozoic atmosphere. Nat. Commun. 9 (1), 4081.
- Kristensen, E., Blackburn, T.H., 1987. The fate of organic carbon and nitrogen in experimental marine sediment systems: influence of bioturbation and anoxia. J. Mar. Res. 45 (1), 231–257.
- Kristensen, E., Penha-Lopes, G., Delefosse, M., Valdemarsen, T., Quintana, C.O., Banta, G.T., 2012. What is bioturbation? The need for a precise definition for fauna in aquatic sciences. Mar. Ecol. Prog. Ser. 446, 285–302.
- Kunzmann, M., Bui, T.H., Crockford, P.W., Halverson, G.P., Scott, C., Lyons, T.W., Wing, B. A., 2017. Bacterial sulfur disproportionation constrains timing of Neoproterozoic oxygenation. Geology 45 (3), 207–210.
- Lenton, T.M., Daines, S.J., Mills, B.J., 2018. COPSE reloaded: An improved model of biogeochemical cycling over Phanerozoic time. Earth-Sci. Rev. 178, 1–28.
- Li, W., Joshi, S.R., Hou, G., Burdige, D.J., Sparks, D.L., Jaisi, D.P., 2015. Characterizing phosphorus speciation of Chesapeake Bay sediments using chemical extraction, ³¹P NMR, and X-ray absorption fine structure spectroscopy. Environ. Sci. Technol. 49 (1), 203–211.
- Liu, J., Pellerin, A., Antler, G., Kasten, S., Findlay, A.J., Dohrmann, I., Røy, H., Turchyn, A. V., Jørgensen, B.B., 2020. Early diagenesis of iron and sulfur in Bornholm Basin sediments: The role of near-surface pyrite formation. Geochim. Cosmochim. Acta 284, 43.60.
- Liu, J., Antler, G., Pellerin, A., Izon, G., Dohrmann, I., Findlay, A.J., Røy, H., Ono, S., Turchyn, A.V., Kasten, S., Jørgensen, B.B., 2021. Isotopically "heavy" pyrite in marine sediments due to high sedimentation rates and non-steady-state deposition. Geology 49 (7), 816–821.
- Lowson, R.T., 1982. Aqueous oxidation of pyrite by molecular oxygen. Chem. Rev. 82 (5), 461-497.
- Luther III, G.W., 1991. Pyrite synthesis via polysulfide compounds. Geochim. Cosmochim. Acta 55 (10), 2839–2849.
- Lyons, T.W., 1997. Sulfur isotopic trends and pathways of iron sulfide formation in upper Holocene sediments of the anoxic Black Sea. Geochim. Cosmochim. Acta 61 (16), 3367–3382.
- Lyons, T.W., Werne, J.P., Hollander, D.J., Murray, R.W., 2003. Contrasting sulfur geochemistry and Fe/Al and Mo/Al ratios across the last oxic-to-anoxic transition in the Cariaco Basin, Venezuela. Chem. Geol. 195 (1–4), 131–157.
- Maki, J.S., 2013. Bacterial intracellular sulfur globules: Structure and function. Microb. Physiol. 23 (4–5), 270–280.
- Malkin, S.Y., Liau, P., Kim, C., Hantsoo, K.G., Gomes, M.L., Song, B., 2022. Contrasting controls on seasonal and spatial distribution of marine cable bacteria (Candidatus Electrothrix) and Beggiatoaceae in seasonally hypoxic Chesapeake Bay. Limnol. Oceanogr. 67 (6), 1357–1373.
- Marvin-DiPasquale, M.C., Capone, D.G., 1998. Benthic sulfate reduction along the Chesapeake Bay central channel. I. Spatial trends and controls. Mar. Ecol. Prog. Ser. 168, 213–228.
- Marvin-DiPasquale, M.C., Boynton, W.R., Capone, D.G., 2003. Benthic sulfate reduction along the Chesapeake Bay central channel. II. Temporal controls. Mar. Ecol. Progr. Ser. 260, 55–70.
- Masterson, A., Alperin, M.J., Berelson, W.M., Johnston, D.T., 2018. Interpreting multiple sulfur isotope signals in modern anoxic sediments using a full diagenetic model (California-Mexico margin: Alfonso Basin). Am. J. Sci. 318 (5), 459–490.

- Meister, P., Liu, B., Ferdelman, T.G., Jørgensen, B.B., Khalili, A., 2013. Control of sulphate and methane distributions in marine sediments by organic matter reactivity. Geochim. Cosmochim. Acta 104, 183–193.
- Meysman, F.J., Middelburg, J.J., Heip, C.H., 2006. Bioturbation: a fresh look at Darwin's last idea. Trends Ecol. Evol. 21 (12), 688–695.
- Middelburg, J.J., 1991. Organic carbon, sulphur, and iron in recent semi-euxinic sediments of Kau Bay, Indonesia. Geochim. Cosmochim. Acta 55 (3), 815–828.
- Middelburg, J.J., Levin, L.A., 2009. Coastal hypoxia and sediment biogeochemistry. Biogeosciences 6 (7), 1273–1293.
- Mills, B.J., Krause, A.J., Jarvis, I., Cramer, B.D., 2023. Evolution of Atmospheric O₂ Through the Phanerozoic. Revisited. Annu. Rev. Earth Planet. Sci. 51, 253–276.
- Milucka, J., Ferdelman, T.G., Polerecky, L., Franzke, D., Wegener, G., Schmid, M., Lieberwirth, I., Wagner, M., Widdel, F., Kuypers, M.M., 2012. Zero-valent sulphur is a key intermediate in marine methane oxidation. Nature 491 (7425), 541–546.
- Moeslund, L., Thamdrup, B., Barker Jørgensen, B., 1994. Sulfur and iron cycling in a coastal sediment: radiotracer studies and seasonal dynamics. Biogeochemistry 27, 129–152.
- Morse, J.W., Wang, Q., 1997. Pyrite formation under conditions approximating those in anoxic sediments: II. Influence of precursor iron minerals and organic matter. Mar. Chem. 57 (3–4), 187–193.
- Newcombe, C.L., Horne, W.A., 1938. Oxygen-poor waters of the Chesapeake Bay. Science 88 (2273), 80–81.
- Nie, Y., Suayah, I.B., Benninger, L.K., Alperin, M.J., 2001. Modeling detailed sedimentary ²¹⁰Pb and fallout ^{239,240}Pu profiles to allow episodic events: An application in Chesapeake Bay. Limnol. Oceanogr. 46 (6), 1425–1437.
- Nielsen, O.I., Kristensen, E., Holmer, M., 2003. Impact of Arenicola marina (Polychaeta) on sediment sulfur dynamics. Aquat. Microb. Ecol. 33 (1), 95–105.
- Nittrouer, C.A., DeMaster, D.J., McKee, B.A., Cutshall, N.H., Larsen, I.L., 1984. The effect of sediment mixing on Pb-210 accumulation rates for the Washington continental shelf. Mar. Geol. 54 (3–4), 201–221.
- Officer, C.B., Lynch, D.R., Setlock, G.H., Helz, G.R., 1984. Recent sedimentation rates in Chesapeake Bay. In: Kennedy, V.S. (Ed.), The Estuary as a Filter. Academic Press, Orlando, Florida, pp. 131–157.
- Palinkas, C.M., Koch, E.W., 2012. Sediment accumulation rates and submersed aquatic vegetation (SAV) distributions in the mesohaline Chesapeake Bay, USA. Estuaries Coast. 35, 1416–1431.
- Pasquier, V., Sansjofre, P., Rabineau, M., Revillon, S., Houghton, J., Fike, D.A., 2017. Pyrite sulfur isotopes reveal glacial – interglacial environmental changes. Proc. Natl. Acad. Sci. 114 (23), 5941–5945.
- Pasquier, V., Bryant, R.N., Fike, D.A., Halevy, I., 2021. Strong local, not global, controls on marine pyrite sulfur isotopes. Sci. Adv. 7 (9), eabb7403.
- Picard, A., Gartman, A., Clarke, D.R., Girguis, P.R., 2018. Sulfate-reducing bacteria influence the nucleation and growth of mackinawite and greigite. Geochim. Cosmochim. Acta 220, 367–384.
- Present, T.M., Adkins, J.F., Fischer, W.W., 2020. Variability in sulfur isotope records of Phanerozoic seawater sulfate. Geophys. Res. Lett. 47 (18), e2020GL088766.
- Pritchard, D.W., 1952. Salinity distribution and circulation in the Chesapeake Bay estuarine system. J. Mar. Res. 11, 106–123.
- Pruss, S.B., Gill, B.C., 2024. Life on the edge: The Cambrian marine realm and oxygenation. Annu. Rev. Earth Planet. Sci. 52.
- Quintana, C.O., Kristensen, E., Valdemarsen, T., 2013. Impact of the invasive polychaete Marenzelleria viridis on the biogeochemistry of sandy marine sediments. Biogeochemistry 115, 95–109.
- Rabalais, N.N., Turner, R.E., Gupta, B.K.S., Platon, E., Parsons, M.L., 2007. Sediments tell the history of eutrophication and hypoxia in the northern Gulf of Mexico. Ecol. Appl. 17 (805). S129–S143.
- Raiswell, R., 1993. Kinetic controls on depth variations in localised pyrite formation. Chem. Geol. 107 (3–4), 467–469.
- Raiswell, R., Hardisty, D.S., Lyons, T.W., Canfield, D.E., Owens, J.D., Planavsky, N.J., Poulton, S.W., Reinhard, C.T., 2018. The iron paleoredox proxies: A guide to the pitfalls, problems and proper practice. Am. J. Sci. 318 (5), 491–526.
- Raven, M.R., Sessions, A.L., Fischer, W.W., Adkins, J.F., 2016. Sedimentary pyrite 8³⁴S differs from porewater sulfide in Santa Barbara Basin: Proposed role of organic sulfur. Geochim. Cosmochim. Acta 186, 120–134.
- Rickard, D.T., 1975. Kinetics and mechanism of pyrite formation at low temperatures. Am. J. Sci. 275 (6), 636–652.
- Rickard, D., 1997. Kinetics of pyrite formation by the H2S oxidation of iron (II) monosulfide in aqueous solutions between 25 and 125 C: The rate equation. Geochim. Cosmochim. Acta 61 (1), 115–134.
- Rickard, D., 2012. Sedimentary pyrite. In: Rickard, D. (Ed.), Sulfidic Sediments and Sedimentary Rocks. Elsevier, pp. 233–285.
 Rickard, D., Luther III, G.W., 1997. Kinetics of pyrite formation by the H2S oxidation of iron
- Rickard, D., Luther III, G.W., 1997. Kinetics of pyrite formation by the H2S oxidation of iron (II) monosulfide in aqueous solutions between 25 and 125 C: The mechanism. Geochim. Cosmochim. Acta 61 (1), 135–147.
- Rickard, D., Luther, G.W., 2007. Chemistry of iron sulfides. Chem. Rev. 107 (2), 514–562. Ridgwell, A., Zeebe, R.E., 2005. The role of the global carbonate cycle in the regulation and evolution of the Earth system. Earth Planet. Sci. Lett. 234 (3–4), 299–315.
- Riedinger, N., Brunner, B., Krastel, S., Arnold, G.L., Wehrmann, L.M., Formolo, M.J., Beck, A., Bates, S.M., Henkel, S., Kasten, S., Lyons, T.W., 2017. Sulfur cycling in an iron oxide-dominated, dynamic marine depositional system: The Argentine continental margin. Front. Earth Sci. 5, 33.
- Riemer, S., Turchyn, A.V., Pellerin, A., Antler, G., 2023. Digging Deeper: Bioturbation increases the preserved sulfur isotope fractionation. Front. Mar. Sci. 9.
- Roden, E.E., Tuttle, J.H., 1992. Sulfide release from estuarine sediments underlying anoxic bottom water. Limnol. Oceanogr. 37 (4), 725–738.
- Roden, E.E., Tuttle, J.H., 1993. Inorganic sulfur cycling in mid and lower Chesapeake Bay sediments. Mar. Ecol. Prog. Ser. 93, 101–118.
- Russ, E., Palinkas, C., 2020. Evolving sediment dynamics due to anthropogenic processes in upper Chesapeake Bay. Estuar. Coast. Shelf Sci. 235, 106596.

- Ruttenberg, K. C. (1990). Diagenesis and burial of phosphorus in marine sediments: Implications for the marine phosphorus budget (Order No. 9034244). Available from ProQuest Dissertations Theses Global. (303844064).
- Sadler, P.M., 1981. Sediment accumulation rates and the completeness of stratigraphic sections. J. Geol. 89 (5), 569–584.
- Schaffner, L. C., Jonsson, P., Diaz, R. J., Rosenberg, R., Gapcynski, P. (1992). Benthic communities and bioturbation history of estuarine and coastal systems: Effects of hypoxia and anoxia. In Marine Coastal Eutrophication (pp. 1001–1016). Elsevier.
- Schippers, A., Jørgensen, B.B., 2001. Oxidation of pyrite and iron sulfide by manganese dioxide in marine sediments. Geochim. Cosmochim. Acta 65 (6), 915–922.
- Schoonen, M.A., 2004. Mechanisms of sedimentary pyrite formation. Spec. Pap. Geol. Soc. Am. 379, 117–134.
- Schoonen, M.A.A., Barnes, H.L., 1991. Reactions forming pyrite and marcasite from solution: I. Nucleation of FeS₂ below 100 C. Geochim. Cosmochim. Acta 55 (6), 1495–1504.
- Scott, A.C., Glasspool, I.J., 2006. The diversification of Paleozoic fire systems and fluctuations in atmospheric oxygen concentration. Proc. Natl. Acad. Sci. 103 (29), 10861–10865.
- Sperling, E.A., Wolock, C.J., Morgan, A.S., Gill, B.C., Kunzmann, M., Halverson, G.P., Macdonald, F.A., Knoll, A.H., Johnston, D.T., 2015. Statistical analysis of iron geochemical data suggests limited late Proterozoic oxygenation. Nature 523 (7561), 451-454.
- Sperling, E.A., Boag, T.H., Duncan, M.I., Endriga, C.R., Marquez, J.A., Mills, D.B., Monarrez, P.M., Sclafani, J.A., Stockey, R.G., Payne, J.L., 2022. Breathless through time: oxygen and animals across Earth's history. Biol. Bull. 243 (2), 184–206.
- Steudel, R. (2003). Inorganic polysulfides S_n^2 and radical anions S_n . In Steudel, R. (Ed.), Topics in Current Chemistry (vol. 231): Elemental Sulfur and Sulfur-Rich Compounds II (pp. 127-152). Springer, Berlin.
- Strauss, H., Bast, R., Cording, A., Diekrup, D., Fugmann, A., Garbe-Schönberg, D., Lutter, A., Oeser, M., Rabe, K., Reinke, D., Teichert, B.M.A., Westernströer, U., 2012. Sulphur diagenesis in the sediments of the Kiel Bight, SW Baltic Sea, as reflected by multiple stable sulphur isotopes. Isot. Environ. Health Stud. 48 (1), 166–179.
- Swider, K.T., Mackin, J.E., 1989. Transformations of sulfur compounds in marsh-flat sediments. Geochim. Cosmochim. Acta 53 (9), 2311–2323.
- Tarhan, L.G., Droser, M.L., Planavsky, N.J., Johnston, D.T., 2015. Protracted development of bioturbation through the early Palaeozoic Era. Nat. Geosci. 8 (11), 865–869.
- Tarhan, L.G., Zhao, M., Planavsky, N.J., 2021. Bioturbation feedbacks on the phosphorus cycle. Earth Planet. Sci. Lett. 566, 116961.
- Teder, A., 1971. The equilibrium between elementary sulfur and aqueous polysulfide solutions. Acta Chem. Scand. 25, 1722–1728.
- Thamdrup, B., Fossing, H., Jørgensen, B.B., 1994. Manganese, iron and sulfur cycling in a coastal marine sediment, Aarhus Bay. Denmark. Geochim. Cosmochim. Acta 58 (23), 5115–5129.
- Thiel, J., Byrne, J.M., Kappler, A., Schink, B., Pester, M., 2019. Pyrite formation from FeS and H₂S is mediated through microbial redox activity. Proc. Natl. Acad. Sci. 116 (14), 6807 6002.
- ThomasArrigo, L.K., Bouchet, S., Kaegi, R., Kretzschmar, R., 2020. Organic matter influences transformation products of ferrihydrite exposed to sulfide. Environ. Sci. Nano 7 (11), 3405–3418.
- Tostevin, R., Mills, B.J., 2020. Reconciling proxy records and models of Earth's oxygenation during the Neoproterozoic and Palaeozoic. Interface Focus 10 (4), 20190137.

- Valesini, F.J., Hallett, C.S., Hipsey, M.R., Kilminster, K.L., Huang, P., Hennig, K., 2019. Peel-Harvey Estuary, Western Australia. In: Wolanski, E., Day, J.W., Elliott, M., Ramachandran, R. (Eds.), Coasts and Estuaries. Elsevier, Amsterdam, pp. 103–120.
- van de Velde, S.J., Hidalgo-Martinez, S., Callebaut, I., Antler, G., James, R.K., Leermakers, M., Meysman, F.J., 2020. Burrowing fauna mediate alternative stable states in the redox cycling of salt marsh sediments. Geochim. Cosmochim. Acta 276, 31-49
- van de Velde, S.J., Dale, A.W., Arndt, S., 2023. Bioturbation and the 5⁵⁶Fe signature of dissolved iron fluxes from marine sediments. R. Soc. Open Sci. 10 (1), 220010.
- van de Velde, S., Meysman, F.J., 2016. The influence of bioturbation on iron and sulphur cycling in marine sediments: a model analysis. Aquat. Geochem. 22, 469–504.
- van de Velde, S., Mills, B.J., Meysman, F.J., Lenton, T.M., Poulton, S.W., 2018. Early Palaeozoic ocean anoxia and global warming driven by the evolution of shallow burrowing. Nat. Commun. 9 (1), 2554.
- Wacey, D., Kilburn, M.R., Saunders, M., Cliff, J.B., Kong, C., Liu, A.G., Matthews, J.J., Brasier, M.D., 2015. Uncovering framboidal pyrite biogenicity using nano-scale CN_{org} mapping. Geology 43 (1), 27–30.
- Wan, M., Schröder, C., Peiffer, S., 2017. Fe(III):S(-II) concentration ratio controls the pathway and the kinetics of pyrite formation during sulfidation of ferric hydroxides. Geochim. Cosmochim. Acta 217, 334–348.
- Wang, Y., Hendy, I.L., Latimer, J.C., Bilardello, D., 2019. Diagenesis and iron paleo-redox proxies: New perspectives from magnetic and iron speciation analyses in the Santa Barbara Basin. Chem. Geol. 519, 95–109.
- Wang, P., Wang, H., Linker, L., Tian, R., 2016. Effects of cross-channel bathymetry and wind direction on destratification and hypoxia reduction in the Chesapeake Bay. Estuar. Coast. Shelf Sci. 178, 168–188.
- Wei, G.Y., Planavsky, N.J., He, T., Zhang, F., Stockey, R.G., Cole, D.B., Lin, Y.B., Ling, H.F., 2021. Global marine redox evolution from the late Neoproterozoic to the early Paleozoic constrained by the integration of Mo and U isotope records. Earth-Sci. Rev. 214, 103506
- Wicks, E.C., Jasinski, D.A., Longstaff, B.J., 2007. Breath of life: Dissolved oxygen in Chesapeake Bay. IAN eNewsletter. The Integration & Application Network of. the University of Maryland Center for Environmental Science.
- Wood, R., Zhuravlev, A.Y., 2012. Escalation and ecological selectively of mineralogy in the Cambrian radiation of skeletons. Earth-Sci. Rev. 115 (4), 249–261.
- Zaback, D.A., Pratt, L.M., Hayes, J.M., 1993. Transport and reduction of sulfate and immobilization of sulfide in marine black shales. Geology 21 (2), 141–144.
- Zhang, J.Z., Millero, F.J., 1993. The products from the oxidation of H₂S in seawater. Geochim. Cosmochim. Acta 57 (8), 1705–1718.
- Zhao, Z., Pang, X., Zou, C., Dickson, A.J., Basu, A., Guo, Z., Pan, S., Nielsen, A.T., Schovsbo, N.H., Jing, Z., Dahl, T.W., 2023. Dynamic oceanic redox conditions across the late Cambrian SPICE event constrained by molybdenum and uranium isotopes. Earth Planet. Sci. Lett. 604, 118013.
- Zimmerman, A.R., Canuel, E.A., 2001. Bulk organic matter and lipid biomarker composition of Chesapeake Bay surficial sediments as indicators of environmental processes. Estuar. Coast. Shelf Sci. 53 (3), 319–341.
- Zopfi, J., Böttcher, M.E., Jørgensen, B.B., 2008. Biogeochemistry of sulfur and iron in Thioploca-colonized surface sediments in the upwelling area off central Chile. Geochim. Cosmochim. Acta 72 (3), 827–843.